SFTSV NSs protein is a novel tick antiviral RNAi response suppressor

Mazigh Fares[1#], Melanie McFarlane[1#], Rhys H. Parry[2#], Rozeena Arif[1#], Andrew T. Clarke[1], Wael Kamel[1], Kelsey Davies[1], Riona Datta-Savage[3], Ulrich Schwarz-Linek[3], Lesley Bell-Sakyi[4], Marine J. Petit[5], Esther Schnettler[6,7,8], Alfredo Castello[1], Alain Kohl[1,9] & Benjamin Brennan[1]*

[1]Medical Research Council–University of Glasgow Centre for Virus Research, Glasgow, G61 1QH, Scotland, UK.
[2]School of Chemistry and Molecular Biosciences, The University of Queensland, St. Lucia 4072, Australia.
[3]Biomedical Sciences Research Complex, University of St Andrews, North Haugh, St Andrews, Scotland, United Kingdom.
[4]Department of Infection Biology and Microbiomes, Institute of Infection, Veterinary and Ecological Sciences, University of Liverpool, Liverpool, L3 5RF, UK.
[5]Microbes, Infection & Immunity, School of Biosciences, Faculty of Health and Medical Sciences, University of Surrey, Guildford, UK
[6]Bernhard-Nocht-Institute for Tropical Medicine, 20359 Hamburg, Germany.
[7]German Centre for Infection Research (DZIF), Partner Site Hamburg-Luebeck-Borstel-Riems, 20359 Hamburg, Germany
[8]Faculty of Mathematics, Informatics and Natural Sciences, University Hamburg, 20148 Hamburg, Germany
[9]Liverpool School of Tropical Medicine, Centre for Neglected Tropical Diseases, Departments of Tropical Disease Biology and Vector Biology, Liverpool, L3 5QA, UK.

[#], joint first authors
*, Correspondence: ben.brennan@glasgow.ac.uk

ORCID:

Mazigh Fares	0000-0002-6003-9244
Melanie McFarlane	0000-0002-8392-2291
Rhys H. Parry	0000-0001-9238-1952
Rozeena Arif	0009-0007-0492-6352
Andrew T. Clarke	0000-0001-7271-3833
Wael Kamel	0000-0002-7625-2648
Kelsey Davies	0009-0009-5624-5983
Riona Datta-Savage	0009-0001-3718-0733
Ulrich Schwarz-Linek	0000-0003-0526-223X
Lesley Bell-Sakyi	0000-0002-7305-0477
Marine Petit	0000-0001-7427-7203
Esther Schnettler	0000-0001-8141-3728
Alfredo Castello	0000-0002-1499-4662
Alain Kohl	0000-0002-1523-9458
Benjamin Brennan	0000-0003-4707-726X

Preprint: https://doi.org/10.1101/2025.08.14.670292

Classification:

Biological Sciences; Microbiology

Keywords:

Bunyavirus, severe fever with thrombocytopenia syndrome virus, tick cell line, arthropod innate immune evasion, protein function, RNA-binding protein, protein-RNA interaction, RNA, host-virus interactions

Abstract

Severe fever with thrombocytopenia syndrome virus (SFTSV) is an emerging tick-borne phenuivirus causing high mortality in humans. While the non-structural protein NSs is dispensable for replication in interferon-deficient mammalian cells, we demonstrate for the first time that NSs is essential for viral replication in tick cells. SFTSV infection triggers canonical Dicer-2-mediated antiviral RNA interference (RNAi) in tick cells, producing virus-derived small interfering RNAs (siRNAs) that target viral transcripts for degradation. We show that NSs functions as a viral suppressor of RNAi by selectively engaging and depleting single-stranded RNAs derived from 22-nucleotide siRNAs, likely limiting their incorporation into RNA-induced silencing complexes (RISC). Complementation with a heterologous RNAi suppressor (p19 protein) partially rescues replication of NSs-deficient virus, validating the RNAi suppressive function of NSs. These findings reveal that successful tick-borne viral replication requires host-specific immune evasion strategies and establish NSs-mediated RNAi suppression as essential for SFTSV persistence in arthropod vectors.

Significance Statement

This study reveals a critical requirement for SFTSV infection that differs between hosts. While the viral NSs protein is dispensable in interferon deficient mammalian cells, it is essential for replication in tick cells, the natural vectors of the virus. We show that NSs functions as a viral RNA silencing suppressor by associating with virus derived small RNAs and limiting their availability to the tick antiviral RNA interference machinery. This provides mechanistic insight into how tick-borne viruses evade arthropod immune defences through engagement of functional siRNAs rather than broad inhibition of RNA interference pathways. Together, these findings demonstrate that SFTSV employs distinct immune evasion strategies in different hosts and identify NSs as a key determinant of vector cell infection.

MAIN TEXT

Severe fever with thrombocytopenia syndrome virus (SFTSV; *Bandavirus dabieense*; *Phenuiviridae*) emerged as a significant threat to human health following its discovery in central China in 2009 (1), where it was identified as the causative agent of a severe haemorrhagic fever syndrome. This tick-borne phenuivirus rapidly gained attention due to its high case fatality rate of 6-30%. Its distinctive clinical presentation is characterized by fever, thrombocytopenia, leukocytopenia, and gastrointestinal manifestations (2). The geographic range of SFTSV has since expanded across East Asia, with confirmed cases reported in South Korea, Japan, Taiwan, and Vietnam, establishing it as a regional public health concern of growing importance (3). Currently, no effective antiviral drugs or vaccines exist to treat SFTS disease.

SFTSV transmission occurs primarily through the bite of infected ixodid ticks, with several species identified as potential vectors (4). *Haemaphysalis longicornis* serves as the principal vector across much of the SFTSV geographical range, while *Haemaphysalis flava* and *Rhipicephalus microplus* may also contribute to transmission cycles in specific regions (5). Ticks acquire SFTSV through blood feeding on infected vertebrate hosts and can subsequently transmit the virus to humans and other susceptible animals. This complex ecology involves multiple tick

species and some amplifying vertebrate hosts (hedgehogs and small rodents), creating diverse transmission pathways that complicate control efforts (6).

Arthropod vectors, including ticks, have evolved sophisticated innate immune mechanisms to combat viral infections, with RNA interference (RNAi) representing a primary antiviral defence pathway (7, 8). Unlike mammals, in which type I interferon responses dominate antiviral immunity (9), arthropods rely heavily on RNAi machinery to recognise and degrade viral nucleic acids. Tick antiviral RNAi responses produce characteristic 22-nucleotide small interfering RNAs (siRNA) through Dicer-2 processing of viral double-stranded RNA intermediates, which are subsequently incorporated into RNA-induced silencing complexes (RISC) to target complementary viral transcripts for degradation (8, 10). Distinguishing authentic virus-derived siRNAs (vsiRNA) from RNA degradation products requires methylation-sensitive approaches, as functional siRNAs undergo Hua Enhancer-1 (HEN1)-mediated 2'-O-methylation upon RISC loading (11-15). The effectiveness of arthropod RNA silencing as an antiviral mechanism has been demonstrated across diverse vector species (flies and mosquitoes) (16), yet our understanding of how tick-borne viruses evade or suppress these responses remains limited (17).

The evolutionary arms race between viruses and RNAi defenses has driven many viruses to evolve suppressors of RNAi (VSRs) that counteract antiviral silencing (18, 19). They employ diverse mechanisms to inhibit RNAi activity, including sequestration of siRNAs, interference with Dicer processing, and disruption of RISC assembly and function. While NSs proteins from plant-infecting tospoviruses are well-characterized RNAi suppressors that bind double-stranded siRNAs (20), vertebrate-infecting bunyaviruses show variable suppressor activities (21). Crucially, no arthropod-specific RNAi suppression mechanisms have been definitively established for tick-borne phenuiviruses.

Despite SFTSV's emergence as a significant public health threat and evidence of vsiRNA production in infected ticks (22), the specific mechanisms by which tick-borne phenuiviruses evade or suppress arthropod RNAi responses remain unknown. While the non-structural protein (NSs) of SFTSV has been suggested as a possible RNAi suppressor (22, 23), its actual role and mechanism of action in arthropod cells have yet to be definitively established.

Here, we demonstrate for the first time that SFTSV exhibits fundamentally different replication requirements in tick versus mammalian cell cultures, with NSs proving essential for viral maintenance in tick cells. Using comprehensive molecular analyses including methylation-sensitive small RNA sequencing, structural modelling, and complementation studies with heterologous suppressors, we reveal that NSs functions as a unique viral suppressor of RNAi by selectively sequestering the pool of virus-derived single stranded siRNAs away from the RNAi machinery, thereby enabling productive infection in tick cells and enhancing vector-borne transmission potential.

149 **RESULTS**

150 **SFTSV infects cell lines derived from tick species reported to act as competent**
151 **vectors.**

152 To identify suitable tick cellular models for SFTSV infection, we tested multiple cell
153 lines representing both *Metastriata* (*Rhipicephalus* and *Hyalomma* spp.) and
154 *Prostriata* (*Ixodes* and *Amblyomma* spp.) lineages of the family *Ixodidae*, using
155 wildtype (wt) SFTSV strain HB29 (SI Appendix, Fig. S1) (1, 24). Viral yield assays
156 revealed SFTSV efficiently replicated in cell lines derived from *Rhipicephalus* and
157 *Hyalomma* spp, evidenced by increased viral titres and nucleocapsid protein
158 detection in infected lysates (SI Appendix, Fig. S1A,B). SFTSV replication was
159 minimal in phylogenetically distinct *Ixodes* and *Amblyomma* spp. tick cell lines,
160 despite these species vectoring other members of the *Phenuiviridae* such as
161 Uukuniemi (25) and Heartland viruses (26, 27). Given that bunyaviruses establish
162 non-cytolytic, continuous viral production in tick cells (25, 28), we monitored
163 infectious virus production daily over 10 days at low MOI (SI Appendix, Fig. S1C).
164 Viral titres steadily decreased over time in *Ixodes* spp. cell lines, but continuous
165 production was evident in *Rhipicephalus* spp. cultures. After 10 days post-infection
166 (dpi), all cultures were split 1:2 and monitored for 14 days; clear SFTSV persistence
167 in BME/CTVM6 and BME/CTVM23 lines (SI Appendix, Fig. S1D) confirms their utility
168 as robust models for studying SFTSV arthropod cell infection (29). These results
169 suggest SFTSV entry and replication may depend on host cellular factors that vary
170 among tick species and demonstrate that permissive cell lines can maintain viable
171 virus over extended culture periods.
172

173 **SFTSV NSs protein expression is repressed in tick cells yet is essential for**
174 **sustained virus replication.**

175 We previously established that SFTSV NSs is a potent interferon antagonist (30) and
176 virulence factor in animal models (31-33). While NSs is essential for replication in
177 interferon-competent mammalian cells, it is dispensable in IFN-deficient cell lines
178 (34), suggesting cell-type-specific functions beyond IFN antagonism. However, the
179 molecular basis for NSs function in tick cells, the natural arthropod vector, has
180 remained unexplored. To address this knowledge gap, we investigated NSs function
181 during SFTSV infection of tick cells. We infected BME/CTVM6 cells, selected for their
182 robust and sustained wt SFTSV replication (SI Appendix, Fig. S1), with either wt or
183 NSs-deleted (delNSs) SFTSV across a range of multiplicities of infection. We
184 observed that wt SFTSV demonstrated stable and abundant production of infectious
185 virus throughout the experiment, with SFTSV titres increasing by approximately 3-
186 $\log_{10}$ FFU/ml over the time course (Fig. 1A). In contrast, delNSs SFTSV failed to
187 maintain infectious progeny, with viral titres declining progressively over the infection
188 time course (Fig. 1B). Consistent with this, Western blot analysis of delNSs SFTSV-
189 infected cell lysates revealed no detectable nucleocapsid protein, indicating
190 complete failure to establish a productive infection in tick cells (Fig. 1C). Notably,
191 NSs protein was undetectable in cells infected with both wt and delNSs SFTSV,
192 despite this protein being detected in mammalian cell controls (Vero E6). This
193 observation was unexpected given the apparent requirement for NSs in tick cells. To
194 investigate this paradox further, we performed immunofluorescence microscopy on
195 infected BME/CTVM6 cells (Fig. 1D). Quantitative analysis revealed that delNSs
196 SFTSV infection led to only 2-8% nucleocapsid-positive cells (Fig. 1E,F). In contrast,

197 60-80% of cells were positive for nucleocapsid protein following wt SFTSV infection
198 across all tested MOIs, demonstrating efficient viral replication (Fig. 1G,H).
199
200 To gain a deeper understanding of the viral protein abundance in SFTSV infected
201 tick cells we performed proteomic analysis of BME/CTVM6 cells infected with wild-
202 type SFTSV at 3- and 6-dpi, examining both the distribution of peptide intensities
203 (Fig. 1I) and mean peptide intensities (Fig. 1J) for viral proteins NSs, nucleocapsid
204 protein (N), glycoprotein precursor (GPC), and RNA-dependent RNA polymerase
205 (RdRp). The peptide intensity distributions for NSs remained unchanged between
206 time points, while N showed a non-significant increase (P = 0.709). This reflects that
207 N protein peptides already exhibited high intensities and broad distribution at 3 dpi,
208 suggesting a detection plateau had been reached. In contrast, GPC and RdRp
209 exhibited significant increases (P = 0.026 and P = 6.23 x 10^{-12}, respectively),
210 indicative of enhanced viral replication and assembly processes (Fig. 1I). Analysis of
211 mean peptide intensities revealed temporal increases for N, GPC, and RdRp from 3
212 to 6 dpi, while NSs maintained the lowest expression levels with minimal temporal
213 change (Fig. 1J). Notably, while NSs-derived peptides were detectable by mass
214 spectrometry, NSs protein intensity levels remained below the detection threshold of
215 Western blot analysis (Fig. 1C), suggesting tightly regulated, low-level expression of
216 this protein. This differential sensitivity between proteomic and immunoblot detection
217 methods reveals that NSs is present but maintained at substantially lower levels
218 compared to structural and replication proteins during SFTSV infection of tick cells.
219

220 **NSs subgenomic mRNA expression is reduced in SFTSV-infected tick cells**
221 **compared to mammalian cells.**

222 The SFTSV NSs protein is encoded within the viral S segment, which employs an
223 ambisense coding strategy to produce both NSs and the N protein, consistent with
224 all phenuiviruses (35). The NSs open reading frame is translated from a subgenomic
225 mRNA transcribed from the antigenomic S RNA template following viral genome
226 replication. To investigate the molecular basis for NSs repression in tick cells, we
227 analysed viral RNA species derived from the S segment during infection of two *R.*
228 *microplus* tick cell lines and compared these results to mammalian Vero E6 cells as
229 controls.
230 We employed Northern blot analysis using strand-specific RNA probes to target
231 either the N or NSs coding regions and to distinguish genomic from antigenomic
232 RNA species (Fig. 1K). Productive viral replication was confirmed in wild-type
233 SFTSV-infected tick cells through detection of both genomic [detected by N(-) and
234 NSs(+) probes] and antigenomic [detected by N(+) and NSs(-) probes] S segment
235 RNA at 6 dpi. While N mRNA was weakly but reproducibly detectable in both tick cell
236 lines and mammalian cell controls, NSs subgenomic mRNA levels were markedly
237 reduced in tick cells compared with Vero E6 cells when probed with the NSs(+)
238 probe (Fig. 1L).
239
240 The observed reduction in NSs subgenomic mRNA levels in tick cells provides a
241 plausible explanation for the diminished NSs protein expression during infection.
242 However, the underlying mechanism, whether due to transcriptional attenuation or
243 altered RNA stability, remains unresolved. While our Northern blot data confirm
244 reduced mRNA accumulation, further investigation is needed to determine whether
245 this reflects regulated transcription termination, selective degradation or post-

transcriptional silencing. This finding also raises important questions about how NSs functions during early infection, before its apparent repression.

SFTSV infection triggers small RNA production in tick cells.

Given that tick cells rely on RNAi as a primary antiviral defence mechanism, we next examined whether wt SFTSV replication, and specifically NSs mRNA, is targeted by the tick RNAi pathway. To determine whether the observed reduction in SFTSV NSs mRNA reflected targeted RNAi-mediated degradation, we used beta elimination to distinguish between RISC-loaded siRNAs, unloaded siRNAs, and RNA degradation products. Small RNA samples were therefore subjected to beta elimination prior to sequencing analysis. This treatment selectively removes degradation fragments and non-methylated siRNAs containing 2',3'-cyclic phosphate termini while preserving HEN1-methylated, RISC-loaded siRNAs bearing 5'-phosphate and 3'-hydroxyl groups (11-15). Since both degradation products and non-RISC-loaded siRNAs exhibit similar size distributions (20-24 nt), protection by HEN1 methylation during beta elimination enables unambiguous identification of functional vsiRNAs and confirms RNAi pathway activation against SFTSV (12, 13).

The effectiveness of beta elimination was validated in uninfected BME/CTVM6 cells (SI Appendix, Fig. S2A), the Ago2-deficient *Aedes aegypti* AF525 cell line (SI Appendix, Fig. S2B), or Semliki Forest virus (SFV)-infected AF525 cells (SI Appendix, Fig. S3A,B) by published methodologies, noting that siRNAs produced by mosquito cells are 21nt in length (11). Following SFTSV infection of BME/CTVM6 cells, approximately 10^5 reads within the small RNA size range (18-30 nt) mapped to each SFTSV genomic segment in untreated samples, with read abundance increasing between 3- and 6-dpi. Although beta elimination reduced overall read counts, the proportional increase in reads mapping to SFTSV RNAs from 3 to 6 dpi was preserved, indicating sustained small RNA responses targeting SFTSV throughout infection (Fig. 2A).

The 5' nucleotide composition of all 22 nt vsiRNAs showed strong bias toward uridine and adenine residues, consistent with arthropod Dicer-2 processing specificity (36). Beta elimination treatment virtually eliminated the 22 nt peak at both time points, indicating these vsiRNAs lacked 3'-terminal methylation and remained susceptible to chemical modification (Fig. 2B,C). Analysis of vsiRNAs mapping to SFTSV genome and antigenome sequences at both 3- and 6-dpi revealed pronounced enrichment for 22 nt species in untreated samples, with comparable distributions observed for genomic and antigenomic reads (Fig. 2D,E). Conversely, longer small RNAs (24-30 nt) were largely unaffected by beta elimination, consistent with 2'-O-methylated piRNAs (PIWI-interacting RNAs; these are small non-coding RNAs, typically 24-31 nucleotides long, that bind to PIWI proteins to regulate gene expression) or degradation fragments that escaped chemical treatment.

Notably, the selective loss of Dicer-2-processed 22 nt reads following beta elimination at 3 dpi demonstrates that the majority of SFTSV-derived siRNAs in BME/CTVM6 cells lack methylation modifications, and remain susceptible to chemical modification (Fig. 2D). However, this transient suppression of vsiRNAs from Ago2 is eventually overwhelmed by 6 dpi, evidenced by the strong 22 nt peak of methylated-vsiRNAs in the beta-eliminated sample, indicating a resumption in the targeting of viral RNA sequences by the RNAi machinery (Fig. 2E).

While HEN1-mediated methylation of RISC-loaded siRNAs is conserved from plants to arthropods (12, 37), the dynamics of this process during viral infection in tick cells

295 have not been previously characterized. Our detection of methylated small RNAs in
296 mock-infected controls (SI Appendix, Fig. S2) and their recovery at 6 dpi confirms
297 that BME/CTVM6 cells possess functional HEN1 methylation machinery. Therefore,
298 markedly reduced levels of methylated SFTSV-specific siRNAs at 3 dpi (Fig. 2D),
299 followed by their subsequent accumulation at 6 dpi (Fig. 2E), indicates active viral
300 suppression of RNAi responses during early infection that is eventually overcome by
301 sustained antiviral pressure, enabling initial viral replication. The observed NSs
302 transcript degradation supports this interpretation (Fig. 1L), demonstrating that
303 functional RNAi activity ultimately prevails despite initial viral evasion mechanisms.
304

305 **RNAi-mediated vsiRNA targeting exhibits temporal dynamics and segment-**
306 **specific preferences across the SFTSV genome.**

307 Given that 22-nt species constituted the predominant small RNA population (which
308 corresponds to the typical length of vsiRNAs produced in tick cells), we mapped
309 vsiRNA coverage across genomic and antigenomic strands of the SFTSV small (S;
310 Fig. 2F), medium (M; Fig. 2G), and large (L; Fig. 2H) segments at 3- and 6-dpi in
311 untreated and beta-eliminated samples. SFV served as a control for beta-elimination
312 efficacy and mapping specificity (SI Appendix, Fig. S3C,D).
313 SFTSV vsiRNA accumulation increased substantially between 3- and 6-dpi across all
314 segments, indicating progressive amplification of the RNAi response. In untreated
315 samples, the M and L segments exhibited extensive targeting, with pronounced
316 accumulation at untranslated regions and segment termini. Beta-elimination
317 confirmed sustained SFTSV targeting by the tick RNAi machinery, demonstrating
318 that observed signals represent authentic vsiRNAs rather than 2'-O-methylated small
319 RNA contaminants. Notably, the S segment displayed concentrated targeting within
320 the intergenic region and the NSs open reading frame on the genomic strand,
321 particularly around the areas previously identified as the transcription termination
322 sites for the N and NSs mRNAs (34), indicating RNAi-mediated cleavage of both
323 genomic RNA and NSs subgenomic transcripts. This finding provides a mechanistic
324 explanation for the reduced NSs mRNA detection observed by Northern blot analysis
325 (Fig. 1L). The strand-specific and segment-preferential targeting patterns
326 demonstrate that tick cells mount a sophisticated, temporally regulated antiviral RNAi
327 response against SFTSV infection, which the wt virus can overcome, whereas a
328 NSs-deletant virus cannot.
329

330 **SFTSV infection triggers canonical Dicer-2-mediated vsiRNA production in tick**
331 **cells.**

332 To characterise the dsRNA cleavage patterns during SFTSV infection, we analysed
333 small RNA overlap profiles and strand complementarity patterns mapping to viral
334 segments at 3- and 6-dpi (Fig. 3). At both timepoints, viral small RNAs predominantly
335 exhibited 20-22 nucleotide lengths with a clear preference for 20 nucleotide overlaps
336 between complementary strands (Fig. 3A,C). Strand overlap analysis revealed
337 enhanced complementarity at positions resulting in 2 nucleotide 3' overhangs,
338 characteristic of canonical Dicer-2 cleavage products (Fig. 3B,D). The average z-
339 score across all three genome segments increased from 1.98 at 3 dpi to 2.54 at 6
340 dpi, suggesting sustained Dicer-2 activity throughout viral replication. Notably, virus-
341 derived small RNAs in the 20-24 nucleotide range all displayed this complementarity
342 pattern across the L, M, and S viral segments, indicating uniform processing.

No evidence of antiviral vpiRNAs (viral PIWI-interacting RNAs) was detected in the expected 24-30 nt range in infected tick cells at either timepoint. As a methodological control, SFV-infected AF525 cells displayed the characteristic sharp 19 nucleotide overlap signature resulting from impaired passenger strand processing in the absence of functional Ago2, along with piRNA signatures in the 24-30 nucleotide range with 10 nucleotide overlaps, as previously documented (11) (SI Appendix, Fig. S4). This contrasts with the broader overlap patterns observed in tick cells, confirming the host species-specific nature of antiviral RNA processing mechanisms.

Viral RNAi suppressor partially rescues replication-defective SFTSV in tick cells.

The findings above suggested that SFTSV NSs functions as an RNA silencing suppressor in tick cells. To test this hypothesis, we engineered a recombinant delNSs SFTSV expressing the tomato bushy stunt virus (TBSV) p19 protein, a well-characterized VSR that sequesters siRNAs to counteract antiviral RNA interference (38, 39). Both delNSs-p19V5 and delNSs-eGFP control viruses replicated efficiently in mammalian Vero E6 cells, confirming viral viability and demonstrating again that NSs is dispensable for replication in IFN-deficient mammalian systems (SI Appendix, Fig. S5).

In contrast, these two viruses showed markedly different phenotypes in tick cells. Wild-type SFTSV established robust infection with abundant viral N protein foci in BME/CTVM6 cells (Fig. 4A), while delNSs-eGFP showed no detectable infection by immunofluorescence (Fig. 4B). Functional complementation with p19 partially rescued this replication defect, enabling limited viral persistence with discrete N protein foci at 6 dpi (Fig. 4C). Quantification of immunofluorescent images demonstrated significantly more N protein-positive cells in delNSs-p19V5 versus delNSs-eGFP infected monolayers, indicating more efficient replication (Fig. 4D). Western blot analysis confirmed increased viral protein expression in delNSs-p19V5 infections, while minimal viral protein was detected in delNSs-eGFP lysates (Fig. 4E). Finally, growth kinetics revealed that delNSs-p19V5 achieved only intermediate replication levels with declining viral titers over time, demonstrating partial but incomplete functional rescue compared to wild-type virus (Fig. 4F). While this represented a modest non-significant improvement over delNSs-eGFP, both mutants remained severely attenuated. These complementation and quantification studies support a role for NSs in counteracting tick antiviral responses. To elucidate the underlying mechanism, we next investigated the biochemical properties of NSs.

SFTSV NSs exhibits structural features consistent with RNA-binding activity.

Given that RNAi often requires direct interaction with RNA substrates, we investigated whether NSs functions as an RNA-binding protein. We generated a high-confidence structural model of the NSs protein using AlphaFold2 (40, 41) (Fig. 5A and SI Appendix, Fig. S6). The predicted structure revealed a compact globular protein with multiple α-helical regions and β-sheet domains. Electrostatic surface analysis demonstrated several distinct positively charged patches distributed across the protein surface (Fig. 5B), a characteristic feature of nucleic acid-binding proteins that facilitates interaction with the negatively charged phosphate backbone of RNA. We next employed computational approaches to identify potential RNA-binding domains (RBDs) within the NSs sequence. RBDetect analysis, which identifies RNA-

binding sites based on sequence homology to known cellular RNA-binding sequences (42, 43), revealed two discrete regions with significant similarity to established RBDs: residues SER13-ARG22 and TRP133-THR141 (Fig. 5C; Dataset S1). The probability scores for RNA-binding activity peaked at approximately 0.9 for the first region and 0.6 for the second region, indicating strong predicted binding potential. To validate these predictions using an independent approach, we applied BindUP analysis, which predicts RNA-binding sites based on surface physicochemical properties (44) (Table S1). This analysis identified a region within α-helix 9 as having high probability for nucleic acid interaction. Notably, when the outputs from both RBDetect and BindUP were mapped onto the AlphaFold2 structural model, the predicted binding sites showed substantial overlap with spatial continuity (Fig. 5D), strengthening confidence in these predictions. Importantly, all identified putative RBDs were located within regions of high structural confidence in the AlphaFold2 model (SI Appendix, Fig. S6E).

SFTSV NSs binds single-stranded 22 nt vsiRNAs in infected cells.

To validate NSs as an RNA-binding protein, we performed immunoprecipitation of V5-tagged p19 and NSs from recombinant virus-infected BME/CTVM6 cells at 2 dpi. Although protein expression levels in whole cell lysates varied between replicates, both proteins were detected in immunoprecipitated samples (Fig. 6A). Small RNA-seq analysis of co-immunoprecipitated RNAs revealed that p19 lysates were enriched for 19-22 nt RNAs as expected (45), whereas NSs immunoprecipitates showed enrichment for 22 nt RNAs (the characteristic products of Dicer-2 processing in tick cells) which comprised 50-55% of all detected reads across three independent replicates (Fig. 6B).

Analysis of small RNA composition demonstrated that 22 nt reads accounted for 75% of mapped reads derived primarily from SFTSV RNA in NSs immunoprecipitates, with approximately 45% from antigenomic sense and 30% from genomic sense sequences. In contrast, p19-associated SFTSV siRNAs were approximately 20nt in length, though this varied between replicates (Fig. 6C; SI Appendix, Fig. S7). When comparing normalized read counts across viral genome segments, both proteins showed similar binding levels, although siRNAs derived from the SFTSV M segment were those most reproducibly immunoprecipitated by NSs across replicates (Fig. 6D).

Genome mapping analysis revealed distinct siRNA mapping patterns between the two proteins. The p19-associated 18-25 nt siRNAs mapped to limited viral genome regions (Fig. 6E, SI Appendix, Fig. S8), whereas NSs-bound 22 nt RNAs mapped to multiple reproducible hotspots distributed across all three viral segments (Fig. 6F, SI Appendix, Fig. S9). Notably, hotspots derived from antigenomic sense S segment RNA corresponded to regions within the genome with strongly predicted secondary structures, such as the siRNA hotspot identified mapping to nt position 1210-1238 of the antigenomic S RNA, which corresponds to the head region of a hairpin structure (Fig. 6F; SI Appendix, Fig. S10).

Crucially, NSs immunoprecipitation revealed a statistically significant reduction (**$p \leq 0.01$) in the proportion of 22 nt siRNA duplex pairs (those with 20 nt overlaps), decreasing from approximately 45% in total infected cell lysates to less than 10% in NSs-bound samples. This reduction was specific to vsiRNAs, as *R. microplus* genome-derived siRNAs showed no difference in duplex abundance (Fig. 6G). Size-specificity analysis confirmed similar single-strand enrichment for 21 nt and 23 nt

siRNAs but not for 24 nt or 28 nt species, demonstrating that NSs selectively binds vsiRNA single strands within a defined size range (SI Appendix, Fig. S11). This sequestration is consistent with post-Dicer processing of vsiRNAs, as correctly processed vsiRNA duplexes were robustly and reproducibly detected in infected tick cells (Fig. 3). These findings support a model in which NSs suppresses RNAi through selective engagement and depletion of single-stranded 22-nt vsiRNAs. The observed reduction in duplex vsiRNA abundance, combined with structural predictions, provides strong support for this mechanism. However, direct evidence of impaired Argonaute loading, such as through Ago2 immunoprecipitation or silencing reporter assays, has yet to be demonstrated. How NSs binding modulates vsiRNA availability to influence RNAi outcomes, thereby permitting productive viral replication, remains to be determined. The molecular details and stoichiometric requirements of NSs–vsiRNA interactions warrant further investigation.

To validate our computational predictions, we performed molecular modelling using authentic 22-nucleotide vsiRNAs identified from NSs immunoprecipitation (Table S2). Docking analyses revealed multiple RNA-binding interfaces within 4Å contact distance for vsiRNAs derived from all three SFTSV genomic segments: S (Fig. 6H), M (Fig. 6I), and L (Fig. 6J).
Notably, the predicted RNA contact residues clustered within the same protein region identified by both RBdetect and BindUP algorithms (Fig. 5D), providing highly convergent evidence for the location of functional RNA-binding sites from orthogonal computational approaches. This structural validation strongly supports the siRNA-binding capacity of SFTSV NSs protein in tick cells and establishes a molecular framework for understanding NSs-mediated RNAi suppression.

To further interrogate the predicted RNA-binding interface of SFTSV NSs, we computationally generated a panel of charge-reversal mutants targeting conserved basic residues within and adjacent to the predicted binding pocket (Table 1; Arg100, Lys105, Arg139, and Lys145). Initial in silico modelling across independent computational approaches, including AlphaFold3-based complex prediction, HADDOCK docking, and iPTM interface confidence analysis, consistently localised RNA interaction to a region spanning residues 100-145 (more strictly between residues 135-144), independent of RNA segment, indicating a stable and well-defined predicted binding site (Fig. 5 and Fig. 6H–J). Confidence in the predicted folding of the mutant NSs structures remained high, indicating there was no overall loss of structure mediated by the mutations (SI Appendix, Fig. S12A). Superposition of the in silico–generated structural models of wild-type NSs with these mutants revealed no substantial changes to the overall fold or local backbone conformation, with the mutated residues occupying equivalent spatial positions in all models. This suggests that the introduced substitutions are not predicted to induce gross structural rearrangement, but rather alter local interface chemistry (SI Appendix, Fig. S12B-E).

We observed reduced protein/RNA interactions particularly with NSs Mutant C and Mutant D, suggesting weakened or less well-defined protein/RNA interfaces (Fig. 7A). We therefore selected these to assess the impact of these mutations on predicted RNA binding using single-stranded vsiRNAs derived from the S (RNA_3), M (RNA_5), and L (RNA_10) genome segments. Across all RNAs, charge-reversal mutations resulted in reduced predicted binding scores and a displacement of the

interaction interface away from the mutated residues, as reflected by concordant reductions in interface confidence (Fig. 7A) and decreases in the predicted interface area and binding free energy across both AlphaFold3 and HADDOCK models (Fig. 7B). Mutations targeting residues within the core 133–145 region had the strongest effects, with Mutant D (Arg139Glu, Lys145Glu) showing the most pronounced and consistent reduction in predicted binding, particularly for M- and L-segment-derived RNAs. Together, these analyses support a model in which NSs engages viral RNAs through a defined, charge-dependent interface centred on residues 133–145, rather than through nonspecific electrostatic interactions.

DISCUSSION

This study reveals a fundamental dichotomy in SFTSV replication strategies between mammalian and arthropod hosts, establishing NSs as a critical viral RNAi suppressor essential for tick cell infection. The striking observation that NSs protein is virtually undetectable in productively-infected tick cells, despite being absolutely required for viral replication, challenges conventional paradigms of viral protein function and highlights the sophisticated evolutionary adaptations that enable arboviral transmission.

The species-specific permissivity patterns observed across tick cell lines (SI Appendix, Fig. S1A,B) provide crucial insights into possible SFTSV vector competence. The successful replication in *R. microplus* cells (BME/CTVM6 and BME/CTVM23) correlates with the known epidemiological distribution of SFTSV-positive ticks, suggesting that cellular factors governing viral entry and replication are phylogenetically conserved traits that determine vector competence in nature. Cell lines from two other species, *Rhipicephalus decoloratus* (BDE/CTVM16) and *Hyalomma anatolicum* (HAE/CTVM9) originating from East Africa and India respectively, also supported SFTSV replication, although the virus has not been reported from these tick species or geographic regions, suggesting the potential for spread beyond its currently known distribution. The sustained viral production over extended culture periods (SI Appendix, Fig. S1C,D) confirms the establishment of infections expected of arthropod-borne bunyaviruses (25, 28, 46, 47). The failure of SFTSV to replicate in *Ixodes* spp. cell lines, despite these ticks vectoring related phenuiviruses (48), indicates that host range determinants may operate at the cellular level.

Here we show that SFTSV NSs protein expression is repressed in tick cells yet is unexpectedly essential for sustained virus replication. This contrasts with mosquito-borne bunyaviruses such as Rift Valley fever virus, where NSs repression does not impact virus replication in mosquito cells and instead facilitates viral persistence (47, 49-51), suggesting distinct host-specific requirements for NSs in different arthropod vectors. The paradoxical requirement for NSs in tick cells represents a remarkable evolutionary balancing act that extends beyond recent findings in mammalian systems (23). Our demonstration that delNSs SFTSV fails to sustain infectious progeny in tick cells (Fig. 1B) and showed no detectable nucleocapsid protein (Fig. 1C), contrasts sharply with dispensable NSs function in IFN-deficient mammalian cells (34). Proteomic analysis revealed differential temporal expression of SFTSV proteins in tick cells, with structural proteins (N, GPC) and the RNA-dependent RNA polymerase (RdRp) showing significant increases from 3 to 6 dpi, while the non-structural protein NSs remained at consistently low levels throughout infection. The detection of NSs by mass spectrometry despite its absence in Western blots suggests tight regulation of this protein in infected tick cells, perhaps compounded by

540 antibody sensitivity (Fig. 1I,J). The paradox of NSs essentiality despite undetectable
541 protein levels may be resolved through several non-exclusive mechanisms. Firstly,
542 based on established proteomics intensity-to-concentration relationships (52, 53),
543 the observed mean peptide intensity for SFTSV NSs (Log2 = 15) suggests protein
544 concentrations in the low nanomolar range (1-10 nM) range, which, while below
545 Western blot detection limits, align with the nanomolar binding affinities characteristic
546 of other viral RNA silencing suppressors (54). While our results support a vsiRNA
547 depletion model, NSs activity is most consistent with interference at or around the
548 RISC engagement stage; however, we cannot yet resolve whether this occurs
549 through effects on vsiRNAs prior to Ago2 loading or through interactions with single-
550 stranded guide RNAs and/or Ago2-containing RISC complexes after loading.
551 Secondly, NSs may exhibit exceptionally high RNA-binding affinity or cooperative
552 binding that amplifies its suppressive capacity at low concentrations. Thirdly,
553 temporal or subcellular compartmentalization may concentrate NSs activity during
554 critical early infection phases, when RNAi activation would otherwise prevent
555 productive replication. The profound replication defect observed in NSs-deficient
556 infections (Fig. 1E,F) reinforces the notion that even low-abundance NSs is
557 functionally essential in tick cells. These mechanisms may collectively explain how
558 limited quantities of NSs achieve effective RNAi suppression in the tick host.
559
560 The selective reduction of NSs subgenomic mRNA in tick cells provides a
561 mechanistic explanation for the protein's low abundance while maintaining its
562 essential function. Our Northern blot analysis (Fig. 1L) demonstrates that while both
563 genomic and antigenomic viral RNAs accumulate to similar levels in tick and
564 mammalian cells, NSs mRNA shows markedly reduced levels specifically in tick
565 cells, suggesting a post-transcriptional regulation mechanism unique to arthropod
566 hosts. This regulatory strategy represents an evolutionary compromise that
567 maximizes NSs activity during critical early infection phases while minimizing
568 detection by host surveillance mechanisms.
569
570 The demonstration that SFTSV infection triggers robust small RNA production in tick
571 cells (Fig. 2A) establishes RNAi as a primary antiviral defence mechanism. Our beta
572 elimination analyses provide definitive evidence that the observed 22-nucleotide
573 small RNAs represent authentic virus-derived siRNAs rather than degradation
574 products (Fig. 2B-E). This finding significantly extends previous work by Xu *et al.*,
575 who demonstrated vsiRNA production during SFTSV infection of whole *H.*
576 *longicornis* ticks through blood feeding (22). Our study advances this understanding
577 by providing detailed mechanistic insights into vsiRNA processing, demonstrating
578 temporal dynamics of the RNAi response, and establishing the functional
579 consequences for viral replication in cell culture systems.
580 The emergence of methylated vsiRNAs at 6 dpi (Fig. 2E), which are absent at 3 dpi,
581 supports a model wherein the host RNAi machinery eventually overcomes transient
582 viral suppression. Given that NSs is expressed at low levels in infected tick cells
583 (undetectable by Western blot; Fig. 1C), complete sequestration of all vsiRNAs
584 would present a significant stoichiometric challenge. This constraint is further
585 amplified by the temporal dynamics of antiviral RNAi responses, as vsiRNA
586 accumulation increases substantially between 3 and 6 dpi. The appearance of RISC-
587 loaded vsiRNAs at 6 dpi therefore indicates that sustained RNAi pathway activation
588 can ultimately saturate the suppressive capacity of this low-abundance viral

589 suppressor, enabling functional antiviral silencing despite initial evasion
590 mechanisms.
591 Our observations support a 'depletion strategy' whereby viral suppressors of RNAi
592 achieve functional suppression without requiring abundant expression. To address
593 potential stoichiometric limitations, we propose that NSs operates through high-
594 affinity binding kinetics rather than simple mass action. Assuming dissociation
595 constants comparable to characterised VSRs [Kd ~0.1-1 nM (54)] and estimated
596 cellular vsiRNA concentrations of 10-100 nM during peak infection, even low-
597 abundance NSs could plausibly compete for substrate binding. Interference with
598 vsiRNAs during RISC engagement, rather than competition with fully assembled
599 RISC complexes, would be expected to be more efficient, providing a conceptual
600 explanation for how limited NSs quantities could achieve functional suppression
601 despite abundant total vsiRNA pools. Such high-affinity interactions are characteristic
602 of other VSRs, including tombusvirus p19, which functions at substoichiometric
603 concentrations (Kd ~0.17 nM) and achieves substantial siRNA depletion despite
604 limited protein abundance (45).
605
606 The progressive amplification of vsiRNA accumulation across all viral segments
607 between 3- and 6-dpi (Fig. 2F-H) indicates that tick cells mount increasingly robust
608 antiviral responses over time. The concentrated targeting within the unencapsidated
609 S segment intergenic region (55) and NSs open reading frame provides direct
610 mechanistic evidence for RNAi-mediated NSs mRNA degradation, explaining the
611 reduced NSs protein levels observed. This segment-specific targeting pattern
612 suggests that viral RNA secondary structures or transcript abundance influence
613 RNAi machinery accessibility, with implications for understanding viral evolutionary
614 constraints.
615
616 The demonstration of canonical Dicer-2-mediated vsiRNA production through strand
617 overlap analysis (Fig. 3) confirms that tick antiviral RNAi pathways follow established
618 arthropod paradigms. The predominance of 20-22 nucleotide products with
619 characteristic 2-nucleotide 3' overhangs indicates uniform processing across all viral
620 segments (8). Notably, the absence of detectable vpiRNA responses contrasts with
621 mosquito antiviral systems (46, 56-59), suggesting lineage-specific adaptations in
622 arthropod small RNA-mediated immunity. However, the complete absence of vpiRNA
623 production warrants further mechanistic investigation to determine whether this
624 reflects genuine pathway absence or differential regulation.
625
626 The successful complementation of NSs-deficient virus with the heterologous p19
627 suppressor (Fig. 4) provides strong evidence that NSs functions as a VSR in tick
628 cells. The partially restored viral protein expression and intermediate replication
629 kinetics in delNSs-p19V5 infected cells demonstrate functional complementation
630 while revealing that NSs possesses unique properties beyond simple siRNA
631 sequestration. This incomplete complementation suggests NSs may: (i) exhibit
632 specific binding preferences for SFTSV-derived vsiRNAs through evolved sequence
633 or structural recognition motifs, (ii) interact with additional host factors beyond the
634 core RNAi machinery, or (iii) function through temporal coordination with other viral
635 proteins during the replication cycle. The heterologous p19 suppressor, while
636 functionally competent, lacks these virus-specific adaptations that have co-evolved
637 to optimise NSs performance within the SFTSV life cycle.
638

Our integrated structural and functional analyses establish NSs as a novel siRNA-binding protein that selectively engages single-stranded 22 nt vsiRNAs through size-specific molecular recognition. This finding extends observations from plant-infecting bunyaviruses, particularly Tospoviruses, where NSs proteins bind both double-stranded siRNAs and miRNAs with varying specificity depending on phylogenetic origin; American clade tospoviruses exhibit broad-spectrum binding, whereas Eurasian clade NSs proteins demonstrate more restricted binding to short dsRNA substrates (20, 60, 61). In these plant-infecting systems, NSs suppresses RNA silencing by binding and sequestering small interfering RNAs, thereby preventing their incorporation into the RNA-induced silencing complex (20, 61, 62). While these observations derive from plant host systems, they suggest that RNA binding-mediated suppression of RNAi may represent a conserved strategy employed by bunyaviral NSs proteins across diverse hosts. Our findings extend this concept to tick cells and support a model in which SFTSV NSs similarly limits antiviral RNAi through interaction with virus-derived small RNAs. Notably, while RNAi suppressor activity has not been clearly demonstrated for NSs proteins from vertebrate-infecting bunyaviruses in either vertebrate hosts or arthropod vectors (20), our results provide strong mechanistic evidence for this function.

Earlier studies implicated SFTSV NSs in modulation of RNA interference primarily through interactions with Argonaute proteins, based on protein–protein interaction data generated in mammalian cells (23) or indirect vsiRNA profiling from whole feeding ticks (22). In contrast, our study directly interrogates NSs function in tick-derived cells and demonstrates association of NSs with single-stranded 22-nt vsiRNAs in the relevant host context. These findings shift the mechanistic focus from Argonaute-centric models toward vsiRNA engagement as a central feature of NSs-mediated RNAi suppression in ticks, providing a plausible explanation for why previous Ago2 co-immunoprecipitation studies detected vsiRNA-associated complexes without resolving functional Argonaute loading. While we cannot exclude additional NSs–Ago2 interactions, our data support a model in which vsiRNA sequestration contributes substantially to RNAi suppression in tick cells. Together, this work defines a tick-specific framework for NSs function that is distinct from mechanisms inferred in mammalian systems and refines our understanding of how SFTSV adapts to the arthropod RNAi pathway.

While our immunoprecipitation and computational modeling provide strong evidence for NSs-vsiRNA interactions, quantitative binding parameters remain to be determined. The inherent challenges associated with NSs biochemical characterization, including insolubility during bacterial expression (24, 63) and extensive C-terminal disorder that complicates *in vitro* folding, have limited direct binding studies. Despite these technical constraints, our cellular interaction data and structural predictions provide compelling concordant evidence for the RNA-binding capacity and size-specific vsiRNA recognition observed in infected tick cells.

The convergence of computational predictions, AlphaFold2 structural modelling (Fig. 5), and experimental data strongly supports a model in which NSs engages virus-derived siRNAs through a defined RNA-binding interface, with discrete binding hotspots suggesting recognition of specific viral RNA secondary structural features (Fig. 6, SI Appendix, Fig. S10). Together with the enrichment of single-stranded 22-nt vsiRNAs in NSs immunoprecipitates, these findings support a model in which NSs

689 suppresses antiviral RNAi through direct engagement of functional vsiRNAs in tick
690 cells. This interaction is most consistent with interference at or around the stage of
691 RISC engagement following Dicer processing, although the precise temporal
692 relationship to Ago2 loading remains to be determined. Future studies employing
693 Ago2 immunoprecipitation or functional RNAi reporter assays will be required to
694 resolve this final mechanistic detail.
695
696 Importantly, our overlap analysis coupled with molecular docking experiments
697 provide strong evidence for the single-stranded nature of the bound RNA substrates,
698 identifying a previously unrecognised mode of RNAi suppression among
699 bunyaviruses that diverges from canonical dsRNA-binding suppressors. The
700 molecular docking validation using authentic vsiRNA sequences derived from viral
701 infections provides direct structural confirmation and establishes a comprehensive
702 molecular framework for understanding NSs-mediated RNAi evasion. This
703 mechanistic insight represents a substantial functional advancement beyond the
704 previous protein-protein interaction studies (NSs/Ago2) conducted in mammalian cell
705 systems.
706
707 The robustness of the proposed mechanism is further supported by the convergence
708 of multiple independent *in silico* analyses, all of which point to a discrete and
709 functionally relevant RNA-binding interface within NSs (Fig. 7, SI Appendix, Fig.
710 S12). The selective sensitivity of RNA binding to charge-reversal mutations argues
711 against nonspecific electrostatic association or global protein destabilisation, and
712 instead supports engagement through a defined, charge-dependent interaction
713 surface. The harmony between distinct computational frameworks, together with
714 functional data obtained in arthropod cells, provides supportive evidence for
715 interface-specific RNA recognition by SFTSV NSs.
716
717 Our findings highlight a key evolutionary adaptation in tick-borne phenuiviruses: the
718 requirement for RNAi suppression in arthropod vectors, but not mammalian hosts.
719 This host-specific dependency likely constrains viral evolution and presents an
720 opportunity for vector-targeted antiviral strategies. The identification of NSs as a
721 siRNA-sequestering protein, rather than an upstream pathway inhibitor, reveals a
722 novel mechanism of immune evasion and offers potential targets for future
723 intervention strategies. Disrupting NSs/vsiRNA interactions or enhancing guide RNA
724 stability could block viral replication in ticks without affecting mammalian infection.
725 While our findings are derived from established tick cell line models, *in vivo*
726 validation in whole *H. longicornis* or *R. microplus* spp. ticks will be essential to
727 confirm the physiological relevance of NSs-mediated RNAi suppression during
728 natural infection. These insights establish NSs as a critical determinant of SFTSV
729 vector competence and uncover a previously unrecognised function for this viral
730 protein.
731

MATERIALS AND METHODS

Tick- and mammalian-cell infection experiments were performed using recombinant SFTSV generated by reverse genetics. Viral replication was assessed by immunofocus assays, immunofluorescence microscopy, Western blotting, Northern blotting and proteomics. Small RNA responses were analysed using methylation-sensitive small RNA sequencing, immunoprecipitation of V5-tagged viral proteins, and computational mapping pipelines. Structural predictions and protein–RNA docking were performed using AlphaFold2/3, HADDOCK, and complementary RNA-binding prediction algorithms. Full experimental procedures and computational pipelines are provided in the SI Appendix.

ACKNOWLEDGEMENTS

We thank Prof. Ulrike Munderloh, University of Minnesota, for permission to use the ISE6, AAE2 and AAE12 cell lines. We also thank Dr Matthew Arnold (Royal Veterinary College) for support with the initial AlphaFold modelling.

FUNDING

This research was funded by a Wellcome Trust/Royal Society Sir Henry Dale Fellowship (210462/Z/18/Z) awarded to B.B. (supporting M.F., M.McF., K.D., A.T.C and B.B.). The facilities used in this study were funded by the UK Medical Research Council (MC_UU_00034/4, MC_UU_00034/8). R.H.P. was supported by a Medical Research Future Fund, Early to Mid-Career Researcher Grant MRF2022950. L.B.S. was supported by the UK BBSRC grant no. BB/P024270/1 and the Wellcome Trust grant no. 223743/Z/21/Z. U.S-L. was funded by MRC grant MR/W018608/1 (supporting R. D-S.). M.J.P. was funded by European Union's Horizon 2020 Research and Innovation Program under the Marie Skłodowska-Curie grant agreement No 890970. E.S. was funded by German Centre for Infection Research (DZIF) (TTU 01.708). A.C. is funded by the European Research Council (ERC) Consolidator Grant 'vRNP-capture' 101001634 and the MRC grants MR/R021562/1 and MC_UU_00034/2 (supporting R.A & W.K.). A.K., was funded by the UK Medical Research Council (MC_UU_12014/8, MC_UU_00034/4). This research was funded in whole or in part by the Wellcome Trust.

The funders had no role in study design, data collection and analysis, decision to publish, or preparation of the manuscript.

AUTHORS' CONTRIBUTIONS

Conceptualization: M.F., M.McF., E.S., A.C., A.K., B.B., Data Curation: M.F., M.McF., R.H.P., R.A., A.T.C., M.P., B.B., Formal Analysis: M.F., M.McF., R.H.P., R.A., A.T.C., W.K., R.D.S., U.S.L., M.P., A.C., A.K., B.B., Funding Acquisition: B.B., Investigation: M.F., M.McF., R.H.P., R.A., A.T.C., W.K., K.D., R.D.S., U.S.L., A.C., A.K., B.B., Methodology: M.F., M.McF., R.H.P., R.D.S., U.S.L., M.P., E.S., B.B., Project administration: B.B., Resources: L.B.S., B.B., Software: R.H.P., W.K., M.P., B.B., Supervision: U.S.L., A.C., A.K., B.B., Validation: M.F., M.McF., R.H.P., R.A., A.T.C., W.K., K.D., R.D.S., U.S.L., M.P., E.S., A.C., A.K., B.B., Visualization: M.F., M.McF., R.H.P., R.A., A.T.C., W.K., B.B., Writing – original draft: M.F., M.McF., A.K.,

B.B., Writing – review & editing: M.F., M.McF., R.H.P., R.A., A.T.C., W.K., K.D., R.D.S., U.S.L., L.B.S., M.P., E.S., A.C., A.K., B.B.

DECLARATION OF INTERESTS

The authors declare no competing interests.

DATA AVAILABILITY

All data that support the findings of this study are openly available from Enlighten Research Data (https://doi.org/10.5525/gla.researchdata.2028). All sequencing data generated in this study have been deposited in the NCBI Sequence Read Archive under BioProject accession number PRJNA1283909. The bioinformatic scripts used for analysis can be found in the Zenodo online repository (https://doi.org/10.5281/zenodo.15877198).

REFERENCES

1. X. J. Yu *et al.*, Fever with thrombocytopenia associated with a novel bunyavirus in China. *N Engl J Med* **364**, 1523-1532 (2011).
2. M. A. Casel, S. J. Park, Y. K. Choi, Severe fever with thrombocytopenia syndrome virus: emerging novel phlebovirus and their control strategy. *Exp Mol Med* **53**, 713-722 (2021).
3. J. C. Li *et al.*, Epidemiology, clinical characteristics, and treatment of severe fever with thrombocytopenia syndrome. *Infect Med (Beijing)* **1**, 40-49 (2022).
4. H. Jang *et al.*, Seasonal dynamics of Haemaphysalis tick species as SFTSV vectors in South Korea. *Microbiol Spectr* **12**, e0048924 (2024).
5. Y. Y. Hu *et al.*, Role of three tick species in the maintenance and transmission of Severe Fever with Thrombocytopenia Syndrome Virus. *PLoS Negl Trop Dis* **14**, e0008368 (2020).
6. L. J. Pérez *et al.*, Ecological Changes Exacerbating the Spread of Invasive Ticks has Driven the Dispersal of Severe Fever with Thrombocytopenia Syndrome Virus Throughout Southeast Asia. *Mol Biol Evol* **41** (2024).
7. G. Barry *et al.*, Gene silencing in tick cell lines using small interfering or long double-stranded RNA. *Exp Appl Acarol* **59**, 319-338 (2013).
8. E. Schnettler *et al.*, Induction and suppression of tick cell antiviral RNAi responses by tick-borne flaviviruses. *Nucleic Acids Res* **42**, 9436-9446 (2014).
9. H. H. Hoffmann, W. M. Schneider, C. M. Rice, Interferons and viruses: an evolutionary arms race of molecular interactions. *Trends Immunol* **36**, 124-138 (2015).
10. D. B. Gammon, C. C. Mello, RNA interference-mediated antiviral defense in insects. *Curr Opin Insect Sci* **8**, 111-120 (2015).
11. C. Scherer *et al.*, An Aedes aegypti-Derived Ago2 Knockout Cell Line to Investigate Arbovirus Infections. *Viruses* **13** (2021).
12. M. D. Horwich *et al.*, The Drosophila RNA methyltransferase, DmHen1, modifies germline piRNAs and single-stranded siRNAs in RISC. *Curr Biol* **17**, 1265-1272 (2007).
13. Z. Yang *et al.*, Approaches for studying microRNA and small interfering RNA methylation in vitro and in vivo. *Methods Enzymol* **427**, 139-154 (2007).
14. S. Alefelder, B. K. Patel, F. Eckstein, Incorporation of terminal phosphorothioates into oligonucleotides. *Nucleic Acids Res* **26**, 4983-4988 (1998).
15. K. Elmer, S. Helfer, M. Mirkovic-Hosle, K. Forstemann, Analysis of endo-siRNAs in Drosophila. *Methods Mol Biol* **1173**, 33-49 (2014).
16. C. D. Blair, K. E. Olson, The role of RNA interference (RNAi) in arbovirus-vector interactions. *Viruses* **7**, 820-843 (2015).
17. A. Wilson *et al.*, Uukuniemi virus infection causes a pervasive remodelling of the RNA-binding proteome in tick cells. *PLoS Pathog* **21**, e1013393 (2025).
18. L. Song *et al.*, Silencing suppressors: viral weapons for countering host cell defenses. *Protein Cell* **2**, 273-281 (2011).
19. J. T. van Mierlo *et al.*, Novel Drosophila viruses encode host-specific suppressors of RNAi. *PLoS Pathog* **10**, e1004256 (2014).
20. M. Hedil, R. Kormelink, Viral RNA Silencing Suppression: The Enigma of Bunyavirus NSs Proteins. *Viruses* **8** (2016).

21. G. Blakqori *et al.*, La Crosse bunyavirus nonstructural protein NSs serves to suppress the type I interferon system of mammalian hosts. *J Virol* **81**, 4991-4999 (2007).
22. Y. Xu *et al.*, Antiviral RNA interference in disease vector (Asian longhorned) ticks. *PLoS Pathog* **17**, e1010119 (2021).
23. N. Javaid, T. W. Jang, Y. Fu, Y. Choi, SFTSV NSs interacts with AGO2 to regulate the RNAi pathway for viral replication. *J Virol* **99**, e0220524 (2025).
24. B. Brennan *et al.*, Reverse genetics system for severe fever with thrombocytopenia syndrome virus. *J Virol* **89**, 3026-3037 (2015).
25. M. Mazelier *et al.*, Uukuniemi Virus as a Tick-Borne Virus Model. *J Virol* **90**, 6784-6798 (2016).
26. E. S. Reynolds, J. T. Wooldridge, H. L. Stevenson, S. Thangamani, The Lone Star tick, Amblyomma americanum, salivary factors exacerbate the clinical outcome of Heartland virus disease in a small animal model. *Sci Rep* **13**, 13304 (2023).
27. L. K. McMullan *et al.*, A new phlebovirus associated with severe febrile illness in Missouri. *N Engl J Med* **367**, 834-841 (2012).
28. M. V. Salvati *et al.*, Virus-Derived DNA Forms Mediate the Persistent Infection of Tick Cells by Hazara Virus and Crimean-Congo Hemorrhagic Fever Virus. *J Virol* **95**, e0163821 (2021).
29. M. J. Petit *et al.*, Multi-omics analysis of SFTS virus infection in Rhipicephalus microplus cells reveals antiviral tick factors. *Nat Commun* **16**, 4732 (2025).
30. V. V. Rezelj *et al.*, Differential Antagonism of Human Innate Immune Responses by Tick-Borne Phlebovirus Nonstructural Proteins. *mSphere* **2** (2017).
31. S. R. Bryden *et al.*, Exploration of immunological responses underpinning severe fever with thrombocytopenia syndrome virus infection reveals IL-6 as a therapeutic target in an immunocompromised mouse model. *PNAS Nexus* **1**, pgac024 (2022).
32. K. M. Yu *et al.*, Cross-genotype protection of live-attenuated vaccine candidate for severe fever with thrombocytopenia syndrome virus in a ferret model. *Proc Natl Acad Sci U S A* **116**, 26900-26908 (2019).
33. Y. Choi *et al.*, Severe fever with thrombocytopenia syndrome phlebovirus non-structural protein activates TPL2 signalling pathway for viral immunopathogenesis. *Nat Microbiol* **4**, 429-437 (2019).
34. B. Brennan, V. V. Rezelj, R. M. Elliott, Mapping of Transcription Termination within the S Segment of SFTS Phlebovirus Facilitated Generation of NSs Deletant Viruses. *J Virol* **91** (2017).
35. R. M. Elliott, B. Brennan, Emerging phleboviruses. *Curr Opin Virol* **5**, 50-57 (2014).
36. M. Reuter *et al.*, The PAZ domain of Aedes aegypti Dicer 2 is critical for accurate and high-fidelity size determination of virus-derived small interfering RNAs. *RNA* **31**, 679-691 (2025).
37. Z. Yang, Y. W. Ebright, B. Yu, X. Chen, HEN1 recognizes 21-24 nt small RNA duplexes and deposits a methyl group onto the 2' OH of the 3' terminal nucleotide. *Nucleic Acids Res* **34**, 667-675 (2006).
38. T. Canto *et al.*, Translocation of Tomato bushy stunt virus P19 protein into the nucleus by ALY proteins compromises its silencing suppressor activity. *J Virol* **80**, 9064-9072 (2006).

894 39. J. W. Park *et al.*, The multifunctional plant viral suppressor of gene silencing
895 P19 interacts with itself and an RNA binding host protein. *Virology* **323**, 49-58
896 (2004).
897 40. J. Jumper *et al.*, Highly accurate protein structure prediction with AlphaFold.
898 *Nature* **596**, 583-589 (2021).
899 41. M. Varadi *et al.*, AlphaFold Protein Structure Database: massively expanding
900 the structural coverage of protein-sequence space with high-accuracy models.
901 *Nucleic Acids Res* **50**, D439-d444 (2022).
902 42. W. Kamel *et al.*, Global analysis of protein-RNA interactions in SARS-CoV-2-
903 infected cells reveals key regulators of infection. *Mol Cell* **81**, 2851-
904 2867.e2857 (2021).
905 43. A. Castello *et al.*, Comprehensive Identification of RNA-Binding Domains in
906 Human Cells. *Mol Cell* **63**, 696-710 (2016).
907 44. I. Paz, E. Kligun, B. Bengad, Y. Mandel-Gutfreund, BindUP: a web server for
908 non-homology-based prediction of DNA and RNA binding proteins. *Nucleic*
909 *Acids Research* **44**, W568-W574 (2016).
910 45. D. Silhavy *et al.*, A viral protein suppresses RNA silencing and binds silencing-
911 generated, 21- to 25-nucleotide double-stranded RNAs. *EMBO J* **21**, 3070-
912 3080 (2002).
913 46. P. Léger *et al.*, Dicer-2- and Piwi-mediated RNA interference in Rift Valley
914 fever virus-infected mosquito cells. *J Virol* **87**, 1631-1648 (2013).
915 47. B. Brennan, S. R. Welch, R. M. Elliott, The consequences of reconfiguring the
916 ambisense S genome segment of Rift Valley fever virus on viral replication in
917 mammalian and mosquito cells and for genome packaging. *PLoS Pathog* **10**,
918 e1003922 (2014).
919 48. A. C. Brault *et al.*, Heartland Virus Epidemiology, Vector Association, and
920 Disease Potential. *Viruses* **10** (2018).
921 49. E. Lara, A. Billecocq, P. Leger, M. Bouloy, Characterization of wild-type and
922 alternate transcription termination signals in the Rift Valley fever virus
923 genome. *J Virol* **85**, 12134-12145 (2011).
924 50. S. Moutailler *et al.*, Replication of Clone 13, a naturally attenuated avirulent
925 isolate of Rift Valley fever virus, in Aedes and Culex mosquitoes. *Vector Borne*
926 *Zoonotic Dis* **10**, 681-688 (2010).
927 51. S. Moutailler *et al.*, Host alternation is necessary to maintain the genome
928 stability of rift valley fever virus. *PLoS Negl Trop Dis* **5**, e1156 (2011).
929 52. T. Geiger *et al.*, Use of stable isotope labeling by amino acids in cell culture as
930 a spike-in standard in quantitative proteomics. *Nat Protoc* **6**, 147-157 (2011).
931 53. B. Schwanhausser *et al.*, Global quantification of mammalian gene expression
932 control. *Nature* **473**, 337-342 (2011).
933 54. J. M. Vargason, G. Szittya, J. Burgyán, T. M. Hall, Size selective recognition of
934 siRNA by an RNA silencing suppressor. *Cell* **115**, 799-811 (2003).
935 55. L. Shalamova *et al.*, Nucleocapsids of the Rift Valley fever virus ambisense S
936 segment contain an exposed RNA element in the center that overlaps with the
937 intergenic region. *Nature Communications* **15**, 7602 (2024).
938 56. C. D. Blair, Deducing the Role of Virus Genome-Derived PIWI-Associated
939 RNAs in the Mosquito-Arbovirus Arms Race. *Front Genet* **10**, 1114 (2019).
940 57. C. Rückert *et al.*, Small RNA responses of Culex mosquitoes and cell lines
941 during acute and persistent virus infection. *Insect Biochem Mol Biol* **109**, 13-
942 23 (2019).

943 58. I. Dietrich *et al.*, RNA Interference Restricts Rift Valley Fever Virus in Multiple
944 Insect Systems. *mSphere* **2** (2017).
945 59. I. Dietrich *et al.*, The Antiviral RNAi Response in Vector and Non-vector Cells
946 against Orthobunyaviruses. *PLoS Negl Trop Dis* **11**, e0005272 (2017).
947 60. S. Eifan *et al.*, Non-structural proteins of arthropod-borne bunyaviruses: roles
948 and functions. *Viruses* **5**, 2447-2468 (2013).
949 61. E. Schnettler *et al.*, Diverging affinity of tospovirus RNA silencing suppressor
950 proteins, NSs, for various RNA duplex molecules. *J Virol* **84**, 11542-11554
951 (2010).
952 62. M. Hedil, D. de Ronde, R. Kormelink, Biochemical analysis of NSs from
953 different tospoviruses. *Virus Res* **242**, 149-155 (2017).
954 63. X. Tao *et al.*, Preparation of a polyclonal antibody against the non-structural
955 protein, NSs of SFTSV. *Protein Expr Purif* **184**, 105892 (2021).
956

FIGURE LEGENDS

Fig. 1. Initial characterisation of wt SFTSV replication in a diverse range of tick cells.

(A-B) Titre of **(A)** wt or **(B)** delNSs SFTSV in the supernatant of infected BME/CTVM6 cells (MOI: 0.1 [grey]; 1 [blue]; or 5 [red]) assayed at the indicated timepoints p.i. Data are plotted as the mean virus titre (FFU/ml) ± SD of n=2 biological replicates.

(C) Representative images of cell lysates derived from cell monolayers in **(A)** and **(B)** harvested at 72 h p.i. As a control, Vero E6 cells were infected with wt SFTSV (MOI: 1) and cell lysates were prepared at 72 h p.i. Western blots were probed with anti-tubulin (loading control), anti-SFTSV NSs or anti-SFTSV N antibodies to detect cellular and viral protein expression. '-ve': mock-infected cell lysate, 'wt': wt SFTSV infected cell lysate, 'delNSs': delNSs SFTSV infected cell lysate. Data show a representative experiment (n=3).

(D) BME/CTVM6 cells seeded onto coverslips were infected with wt- or delNSs- SFTSV at the indicated MOI and were imaged at the timepoints indicated using DAPI (blue) and anti-SFTSV N (red). Imaging was carried out using a Zeiss LSM 880 Confocal Microscope, scale bar is equal to 50 µm.

(E) Percentage of BME/CTVM6 cells infected with delNSs SFTSV (MOI: 0.1 [grey]; 1 [blue]; or 5 [red]) at the timepoints indicated, evidenced by positive staining with anti-SFTSV N antibody. Data are plotted as the mean percent SFTSV-positive cells ± SD of n=3 randomised fields of view.

(F) Number of nuclei enumerated per field of view in (E). Data are plotted as the mean number of nuclei observed ± SD of n=3 randomised fields of view.

(G) Percentage of BME/CTVM6 cells infected with wt SFTSV (MOI: 0.1 [grey]; 1 [blue]; or 5 [red]) at the timepoints indicated, evidenced by positive staining with anti-SFTSV N antibody. Data are plotted as the mean percent SFTSV-positive cells ± SD of n=3 randomised fields of view.

(H) Number of nuclei enumerated per field of view in (G). Data are plotted as the mean number of nuclei observed ± SD of n=3 randomised fields of view.

(I) Violin plot showing peptide intensity distributions (y-axis: Log_2) for wt SFTSV-infected BME/CTVM6 cells at 3- and 6-dpi. Examining peptides derived from non-structural protein (NSs; AJD86041), nucleocapsid protein (N; AJD86040), glycoprotein precursor (GPC; AJD86039) or RNA-dependent RNA polymerase (RdRp; AJD86038). Data taken from n=4 biologically independent replicates.

(J) Bar Chart showing mean peptide intensities (y-axis: Log_2) for same data set presented in (I).

(K) Schematic of SFTSV S genomic RNA configuration showing DIG-labelled probe binding regions used in (L). Probes detect viral genomic (−) or antigenomic (+) sense RNA as indicated. Double-ended arrows indicate genomic replication; single-ended arrows indicate transcription. Black circles indicate 5′ cap structures on mRNAs.

(L) Northern blot analysis of viral RNAs in infected cells. BME/CTVM6 and BME/CTVM23 cells were infected with wt SFTSV (MOI: 0.1) and total RNA was extracted at 6 dpi. Vero E6 cells infected with wt SFTSV were used as a positive control (RNA extracted at 72 h p.i.). DIG-labelled probes complementary to N or NSs coding sequences detected viral genomic (−) or antigenomic (+) sense RNAs. RNA sizes are indicated on the right.

Fig. 2. SFTSV infection of tick cells triggers canonical antiviral RNA interference (RNAi) and production of 22-nt virus-derived small interfering RNAs (vsiRNAs).

BME/CTVM6 cells were infected with wt SFTSV (MOI: 0.1) and total cellular RNA was extracted from infected cells at 3 (light shade) or 6 (dark shade) dpi. Following RNA extraction, samples were either left untreated or processed in a beta-elimination assay, then subjected to small RNA sequencing. β-elimination selectively removes non-methylated RNA fragments while leaving 2'-O-methylated, RISC-loaded vsiRNAs intact, enabling functional siRNAs to be distinguished from degradation products.

(A) Total number of small RNA reads (18-30 nt) in infected cells at 3 (light shading) and 6 (dark shading) dpi. mapping to each wt SFTSV genome segment in untreated samples (left) or beta-eliminated samples (right). SFTSV genome segments: S (KP202165), M (KP202164), L (KP202163). An increase in viral small RNA reads indicates activation of antiviral RNAi over time.

(B) Histogram of all small RNA reads (18-30nt) from untreated (left) or beta-eliminated (right) samples from infected cells at 3 dpi. Read counts are coloured by the identity of the 5′ nucleotide and grouped by read length. Data are shown as the mean percentage of total mapped reads (y-axis); representative of n=3 biologically independent samples.

(C) As per (B), but RNAs were extracted from wt SFTSV-infected cells at 6 dpi. At 6 dpi, a pronounced 22-nt peak re-emerges, indicating accumulation of methylated vsiRNAs that have entered Argonaute-containing RISC complexes.

(D) Histogram of small RNA reads (18-30 nt) from untreated (left) or beta-eliminated (right) samples, mapped to the combined SFTSV antigenomic (positive values) and genomic (negative values) strand RNAs in infected cells at 3 dpi. Read counts are coloured by the identity of the 5′ nucleotide and grouped by read length. Data are shown as the mean percentage of total mapped reads (y-axis); representative of n=3 biologically independent samples.

(E) As per (D), but RNAs were extracted from wt SFTSV-infected cells at 6 dpi. Loss of the 22-nt signal after β-elimination confirms that early vsiRNAs are not yet methylated or RISC-loaded, while its recovery at 6 dpi demonstrates canonical RNAi activation.

(F-H) Mapping of SFTSV-derived 22 nt vsiRNAs (reads per million) across the **(F)** S, **(G)** M, and **(H)** L genome segments at 3 (left) and 6 (right) dpi in BME/CTVM6 cells. Data show antigenomic (blue) and genomic (pink)

sense strands for untreated (top) or beta-eliminated samples (bottom) to remove 2'-O-methylated small RNAs. Numbers indicate nucleotide positions (nt). SFTSV genome segments: S (KP202165), M (KP202164), L (KP202163). Dashed lines represent the boundaries of viral open reading frames and untranslated/intergenic regions. Concentrated vsiRNA peaks within the S segment intergenic region and NSs open reading frame correspond to targeted degradation of viral RNAs by the tick RNAi machinery.
Together, these data demonstrate that SFTSV infection activates Dicer-2–mediated processing of viral RNA into 22-nt vsiRNAs, which progressively acquire methylation and RISC loading as infection proceeds.

Fig. 3. SFTSV virus-derived siRNAs exhibit the canonical 2-nt 3' overhang signature of Dicer-2 processing.

Reanalysis of data from Fig. 2. Dicer-2 processes double-stranded viral RNA into 20–22 nt duplexes with characteristic 2-nucleotide 3' overhangs on each strand, a hallmark of antiviral RNA interference in arthropods.
(A,C) Distribution of overlapping 22 nt vsiRNA pairs by nucleotide overlap length across S (left), M (middle), and L (right) genome segments (normalized per million mapped SFTSV reads). A peak at 2-nt overlap reflects precise Dicer-2 cleavage products.
(B,D) Heat maps showing overlap probability z-scores for vsiRNAs of different lengths (x-axis) and overlap positions (y-axis) from three independent samples. Black boxes highlight the characteristic 2 nt overlap signature of Dicer-2 processing. Colour scale represents z-score values from -4 (teal) to +4 (purple).
(A,B) data from 3 dpi. and **(C,D)** data from 6 dpi.
The increase in overlap z-scores from 3 to 6 dpi indicates sustained Dicer-2 processing and amplification of antiviral vsiRNA production. Absence of 24–30 nt 'ping-pong' overlaps confirms that the tick antiviral response operates via the siRNA, not the piRNA, pathway.

Fig. 4. TBSV p19 protein rescues delNSs SFTSV replication in BME/CTVM6 cells.

BME/CTVM6 cells infected with **(A)** wt SFTSV, **(B)** delNSs-eGFP or **(C)** delNSs-p19V5 virus (MOI: 10). At 6 dpi, cells were fixed and immunostained for SFTSV N protein (red) and nuclei (DAPI, blue). Imaging was carried out using a Zeiss LSM 880 Confocal Microscope, scale bar is equal to 50 µm. **(D)** (Left panel) Percentage of BME/CTVM6 cells infected with wt SFTSV (teal), delNSs-eGFP (red) or delNSs-p19V5 virus (purple) quantified from **(A-C)** at the timepoints indicated, evidenced by positive staining with anti-SFTSV N antibody. Data are plotted as the mean percent SFTSV-positive cells ± SD of n=3 randomised fields of view. (Right panel) Number of nuclei enumerated per field of view from left panel. Data are plotted as the mean number of nuclei observed ± SD of n=3 randomised fields of view. **(E)** Western blot analysis of viral protein expression in infected BME/CTVM6 cells (6 dpi, MOI: 10) and control Vero E6 cells (72 h p.i., MOI: 1). Blots were probed with antibodies against tubulin (loading control), SFTSV NSs, SFTSV N, or V5 tag. Lane labels: wt, wild-type SFTSV; G, delNSs-eGFP; p19, delNSs-p19V5. **(F)** Viral replication kinetics (MOI: 0.1) in BME/CTVM6 cells infected with wt SFTSV (teal), delNSs-p19V5 (red), or delNSs-eGFP (black) viruses. Virus titres were determined by focus-forming assay at indicated time points. Data show one representative experiment from n=3 independent repeats. Statistical analysis was performed using an ordinary one-way ANOVA, with Tukey's multiple comparison test, with a single pooled variance. Asterisks indicate significance: * $p \leq 0.05$, ** $p \leq 0.01$; ns = not significant.

Fig. 5. AlphaFold structural prediction reveals putative nucleic acid binding domains in SFTSV NSs protein.

Predicted three-dimensional structure of SFTSV NSs protein (NCBI Protein: AJD86041).
(A) Surface representation coloured by pLDDT confidence scores: very high confidence (dark blue, 90-100), confident (light blue, 70-89), low confidence (yellow, 50-69), very low confidence (orange, 0-49).
(B) Electrostatic surface potential showing positive (blue) and negative (red) charges.
(C) RNA-binding site prediction using RBDetect analysis. Plot shows probability of RNA binding (y-axis) versus amino acid position (x-axis). Regions between dotted lines indicate high predicted RNA-binding propensity.
(D) Predicted RNA-binding residues mapped onto the protein surface: RBDetect predictions (dark green) and BindUP predictions (light green).

Fig. 6. SFTSV NSs binds viral single-stranded RNA in infected BME/CTVM6 cells.

(A) Immunoprecipitation of V5-tagged NSs proteins to assess NSs-vsiRNA interactions during SFTSV infection. BME/CTVM6 cells infected with SFTSV expressing either deletion mutant NSs-p19V5 (delNSs-p19V5) or wild-type V5-tagged NSs (wt-NSsV5) were harvested at 2 dpi and subjected to immunoprecipitation using anti-V5 antibody. Whole cell lysates (WCL; input) and immunoprecipitates (IP) were analysed by Western blot using anti-tubulin (loading control) and anti-V5 antibodies. RNA was subsequently extracted from immunoprecipitates for small RNA sequencing analysis. Molecular weights (kDa) are indicated. Data represent n=3 biological replicates (Replicate 1-3).
(B) Histogram of all small RNA reads (18-30 nt) in immunoprecipitated samples, p19V5 i.p. (left panel) or NSsV5 i.p. (right panel) representative of n=3 biological replicates.
(C) Small RNA reads from (B) mapped to SFTSV antigenomic (positive values) and genomic (negative values) strand RNAs from p19V5 i.p. (left panel) and NSsV5 i.p. (right panel) samples at 2 dpi. Read counts are coloured by the identity of the 5′ nucleotide and grouped by read length. Data are shown as the mean percentage of total mapped reads (y-axis); representative of n=3 biological replicates.

(D) Distribution of small RNA reads (18-30 nt) mapping to SFTSV genome segments from p19V5 i.p. (left panel) and NSsV5 i.p. (right panel) samples at 2 dpi Data represent n=3 biological replicates.
(E) Mapping of 18-25 nt SFTSV-derived vsiRNAs across the S (left panel), M (middle panel), and L (right panel) genome segments in p19V5 i.p. samples (reads per million). Data show mapping to the SFTSV antigenomic (blue) or genomic (pink) strands; numbers indicate nucleotide positions. Representative data from n=3 biological replicates.
(F) Mapping of 22-nt SFTSV-derived vsiRNAs across genome segments in NSsV5 i.p. samples, as described in (C). Representative data from n=3 biological replicates.
(G) Histogram showing the percentage of 22-nt small RNA reads with 20-nt complementary overlap mapping to SFTSV genome or *R. microplus* genome (GCA_002176555.1) in whole cell lysate (WCL) and NSsV5 i.p. samples. Data represent n=3 biological replicates. Statistical analysis was performed using Brown-Forsythe and Welch's ANOVA with Dunnett's T3 multiple comparison test to compare percentage of RNA reads in duplexes between samples. Asterisks indicate significance: * $p \leq 0.05$, ** $p \leq 0.01$; ns = not significant.
(H-J) AlphaFold3-predicted structure of SFTSV non-structural protein NSs, shown as ribbon and surface representation (grey) bound to single-stranded viral small interfering RNA (vsiRNA, blue) generated during SFTSV infection of BME/CTVM6 tick cells (Fig. 6F) derived from the viral **(H)** S, **(I)** M and **(J)** L segments. Critical amino acids involved in RNA/protein binding to distances <4 Å are highlighted (brown). Green regions highlight key RNA-binding domains identified by RBDetect (Fig. 5C,D).

Fig. 7. Effect of protein mutations on viral siRNA binding predicted through structural modelling.
(A) Mean interface predicted TM-score (iPTM) values for interactions between the wild-type protein (wt NSs) or mutant variants (Mutant A–D) and vsiRNAs derived from the S, M, or L genome segments. Bars represent the mean iPTM score calculated from five AlphaFold3 models per complex, with error bars indicating standard deviation. Individual data points show iPTM scores from each AlphaFold3 model.
(B) Relationship between protein–RNA interface area and interface solvation free energy (ΔiG) calculated using PDB ePISA for wild-type and mutant complexes. Circles denote AlphaFold3-derived complexes (AF3) and squares denote HADDOCK-derived complexes (HAD). Colours indicate protein variants (wt NSs, grey; Mutant A, purple; Mutant B, red; Mutant C, blue; Mutant D, orange). Dashed lines connect AlphaFold and HADDOCK predictions for the same protein–RNA pair.
Reduced iPTM scores, smaller interface areas, and less favourable ΔiG values in mutant complexes indicate weakened protein–RNA binding compared with the wild-type protein.

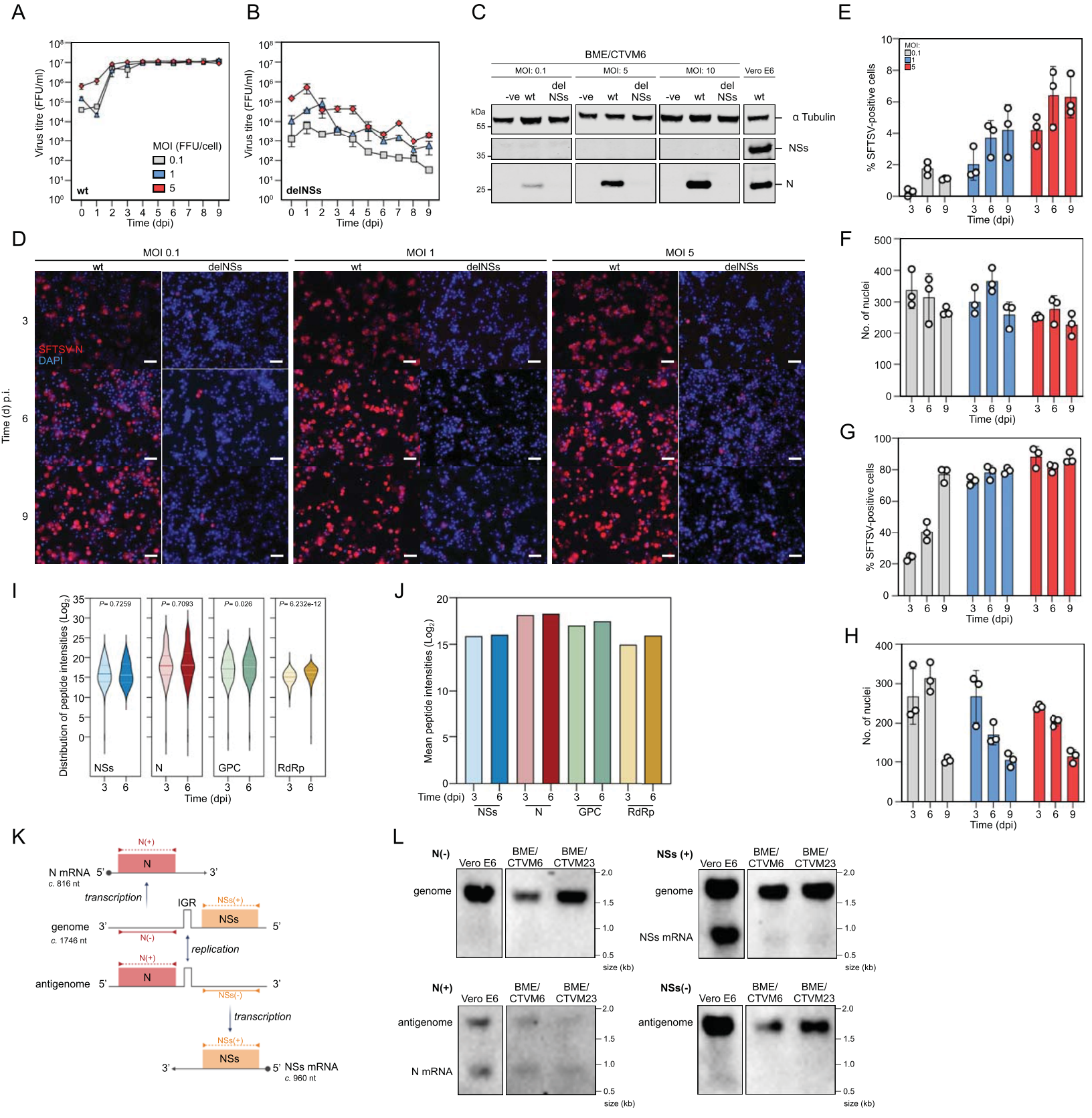
A
B
C
D
E
F
G
H
I
J
K
L
Virus titre (FFU/ml)
Time (dpi)
MOI (FFU/cell)
0.1
1
5
wt
delNSs
BME/CTVM6
MOI: 0.1
MOI: 5
MOI: 10
Vero E6
-ve
del NSs
kDa
α Tubulin
NSs
N
MOI 0.1
MOI 1
MOI 5
SFTSV-N
DAPI
Time (d) p.i.
% SFTSV-positive cells
No. of nuclei
Distribution of peptide intensities (Log2)
Mean peptide intensities (Log2)
P= 0.7259
P= 0.7093
P= 0.026
P= 6.232e-12
GPC
RdRp
N mRNA
c. 816 nt
transcription
IGR
genome
c. 1746 nt
replication
antigenome
NSs mRNA
c. 960 nt
N(+)
N(-)
NSs(+)
NSs(-)
size (kb)
NSs mRNA

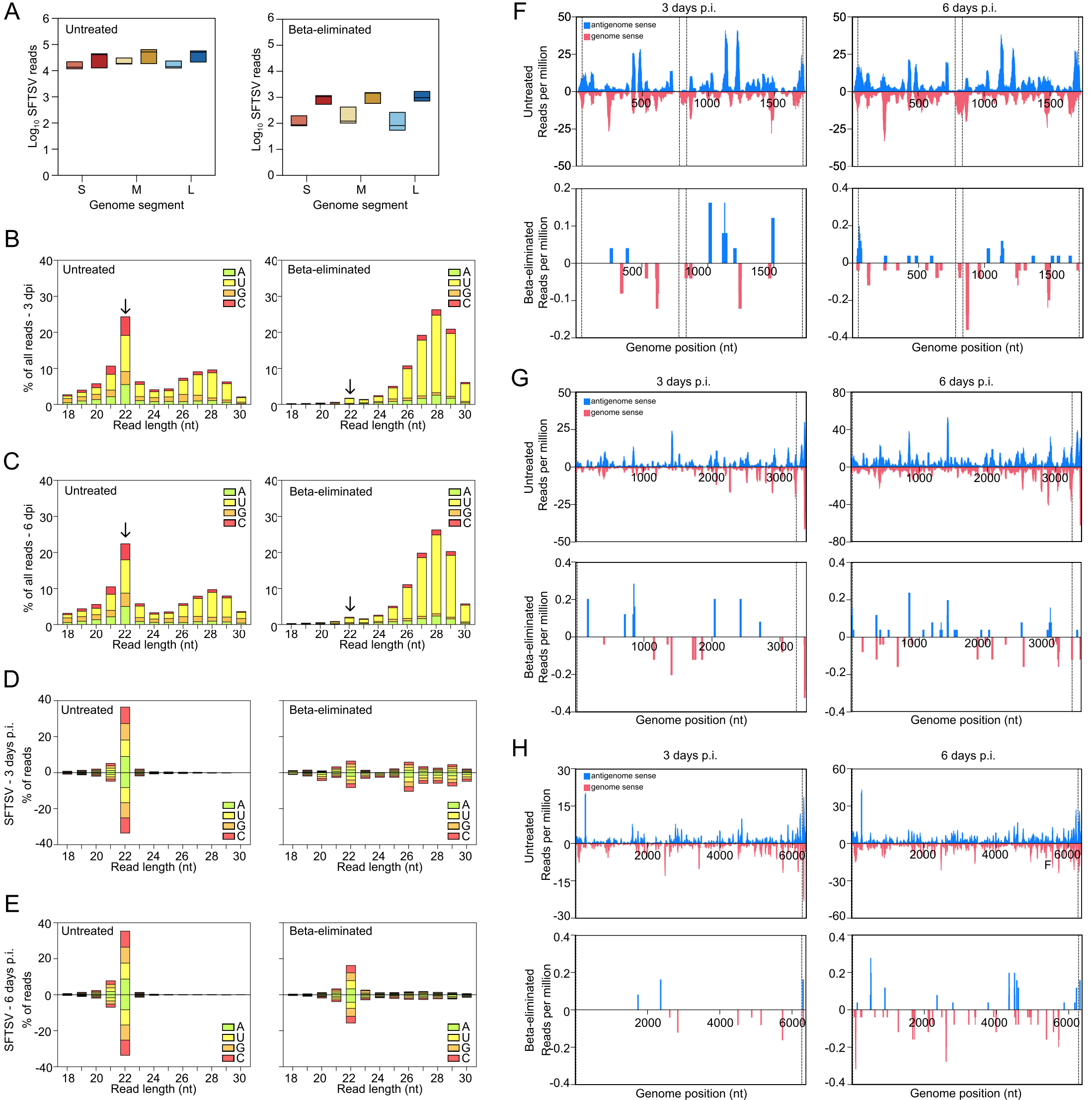
A
Untreated
Beta-eliminated
Log10 SFTSV reads
S
M
L
Genome segment
B
Untreated
Beta-eliminated
% of all reads - 3 dpi
A
U
G
C
Read length (nt)
C
% of all reads - 6 dpi
D
SFTSV - 3 days p.i.
% of reads
E
SFTSV - 6 days p.i.
F
3 days p.i.
6 days p.i.
antigenome sense
genome sense
Untreated
Reads per million
Beta-eliminated
Genome position (nt)
G
H

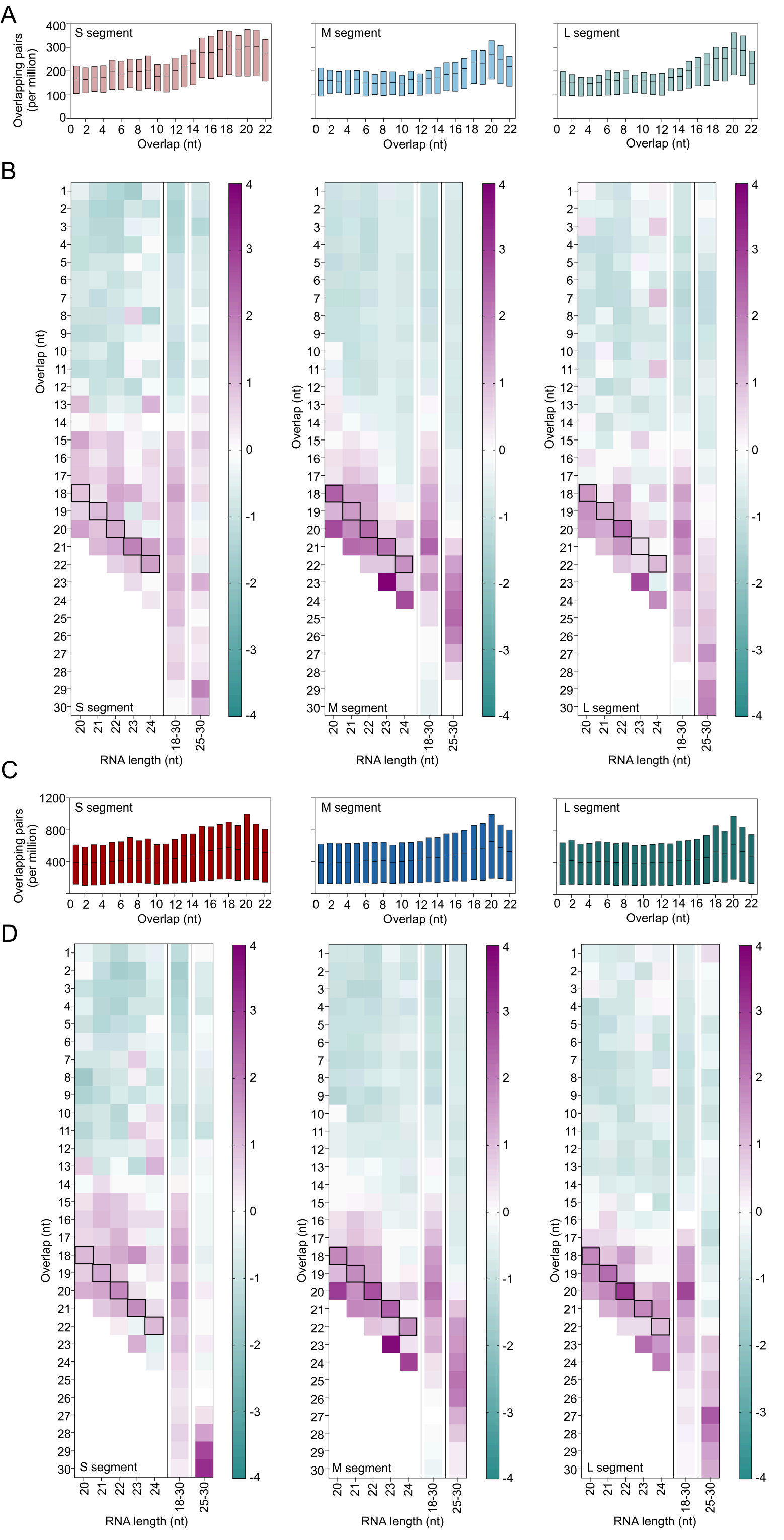
A
S segment
M segment
L segment
Overlapping pairs (per million)
Overlap (nt)
B
Overlap (nt)
RNA length (nt)
C
D

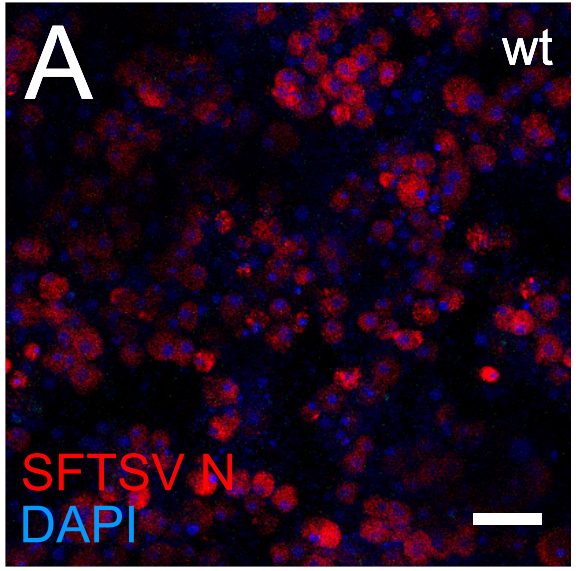
A
wt
SFTSV N
DAPI

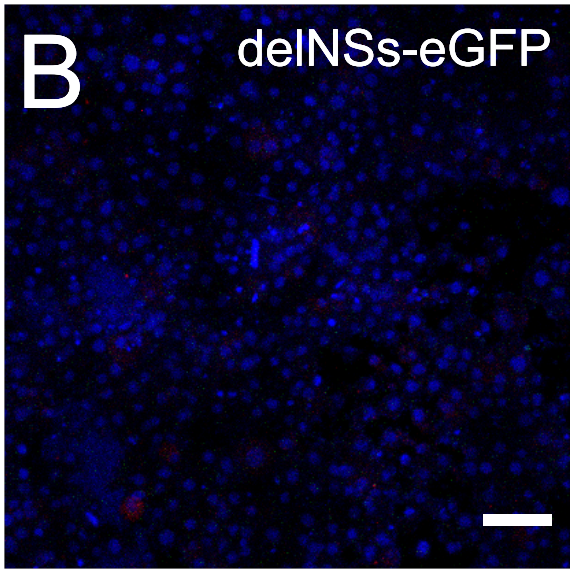
B
delNSs-eGFP

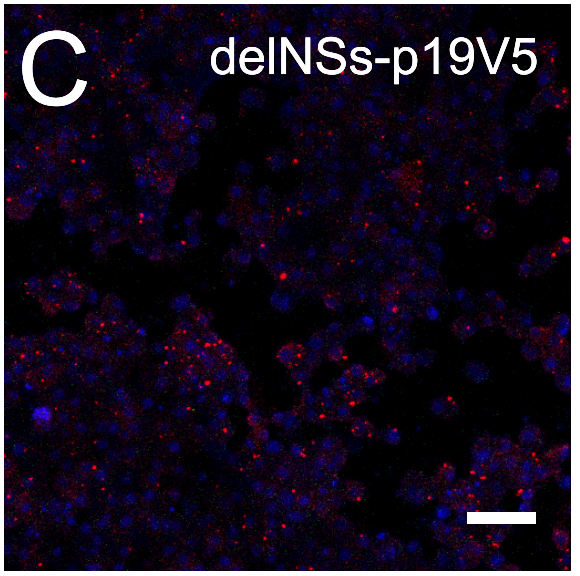
C
delNSs-p19V5

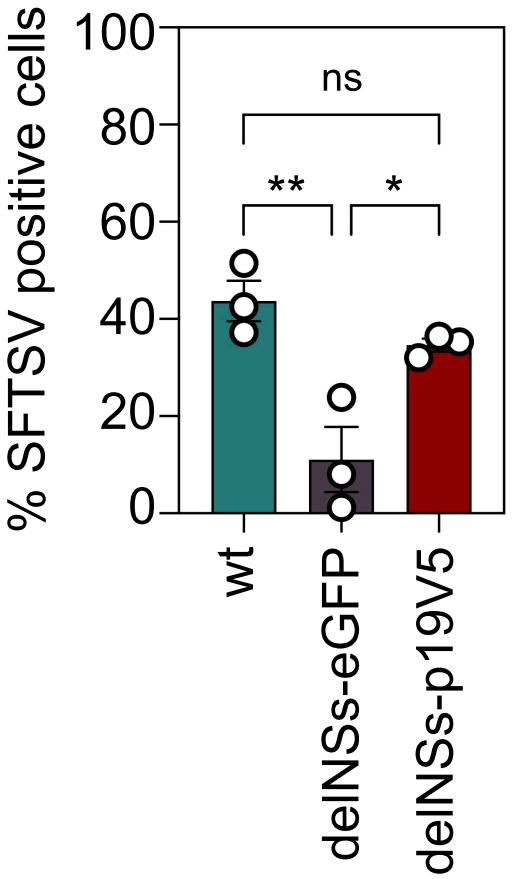
D
% SFTSV positive cells
100
80
60
40
20
0
ns
**
*
wt
delNSs-eGFP
delNSs-p19V5

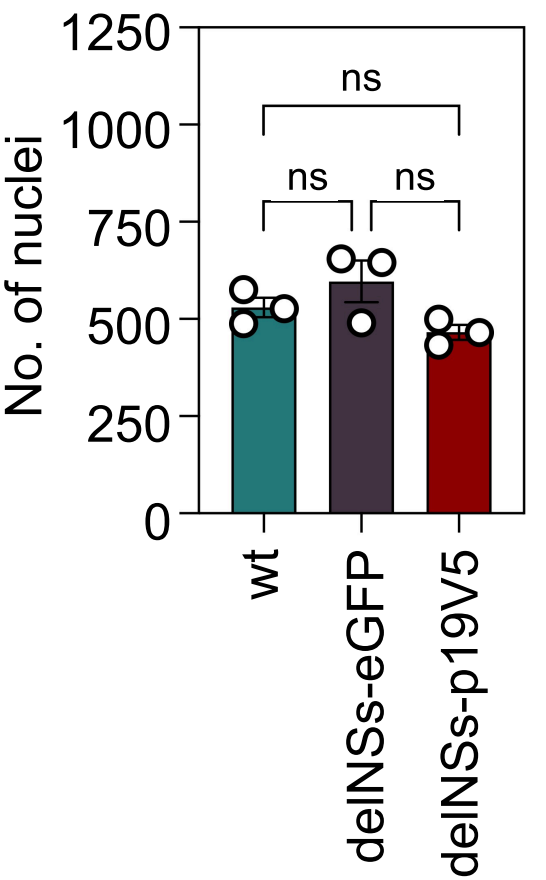
No. of nuclei
1250
1000
750
500
250
0
ns
ns
ns
wt
delNSs-eGFP
delNSs-p19V5

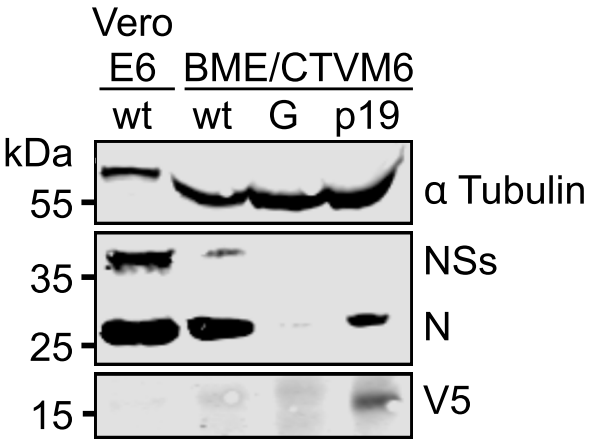
E
Vero
E6
BME/CTVM6
wt
wt
G
p19
kDa
55
35
25
15
α Tubulin
NSs
N
V5

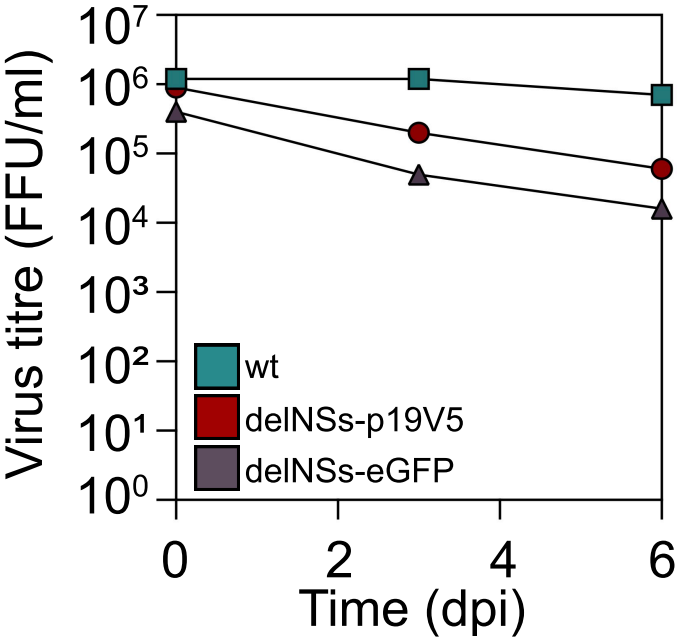
F
Virus titre (FFU/ml)
10^7
10^6
10^5
10^4
10^3
10^2
10^1
10^0
wt
delNSs-p19V5
delNSs-eGFP
0
2
4
6
Time (dpi)

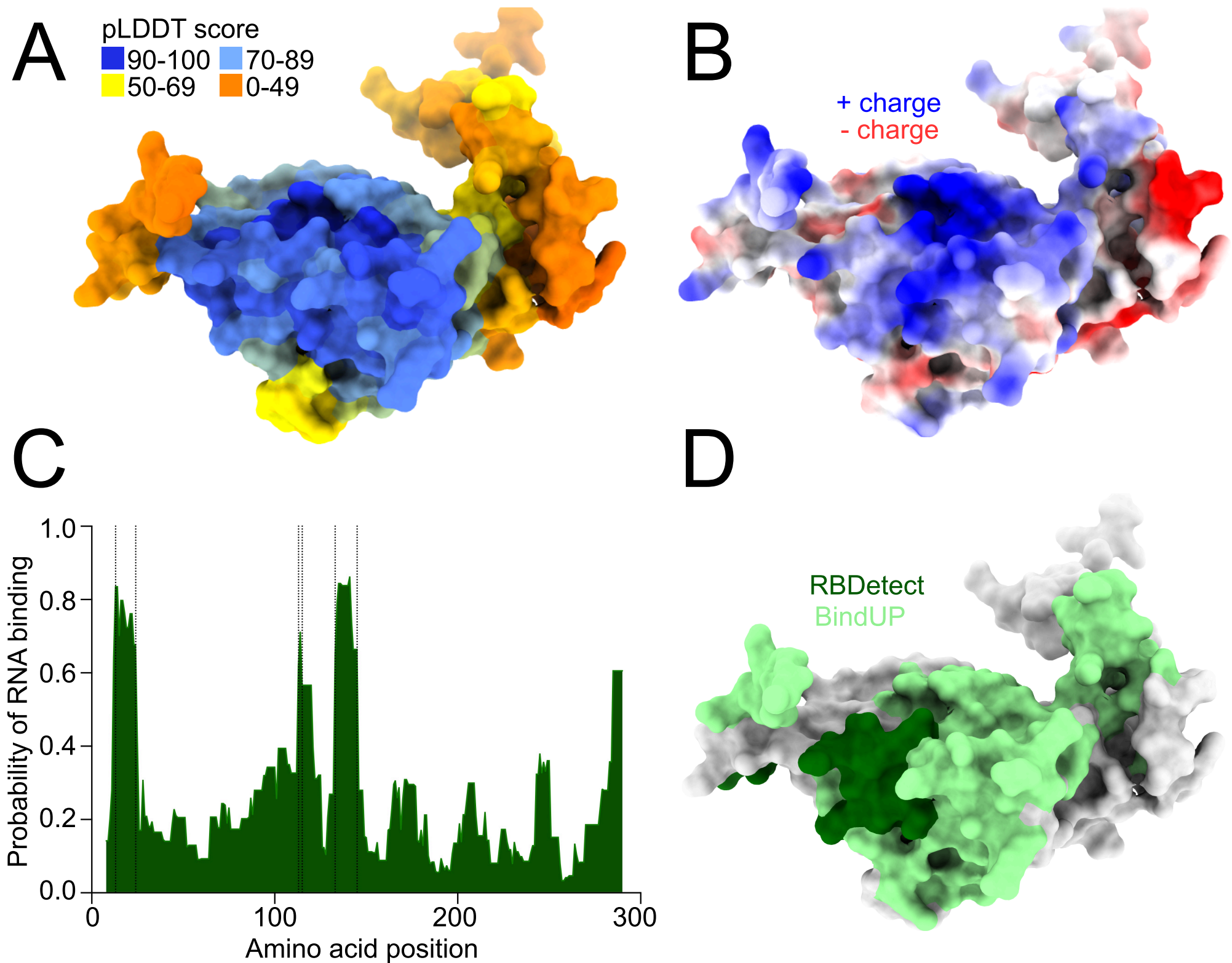
A
pLDDT score
90-100
70-89
50-69
0-49
B
+ charge
- charge
C
Probability of RNA binding
1.0
0.8
0.6
0.4
0.2
0.0
0
100
200
300
Amino acid position
D
RBDetect
BindUP

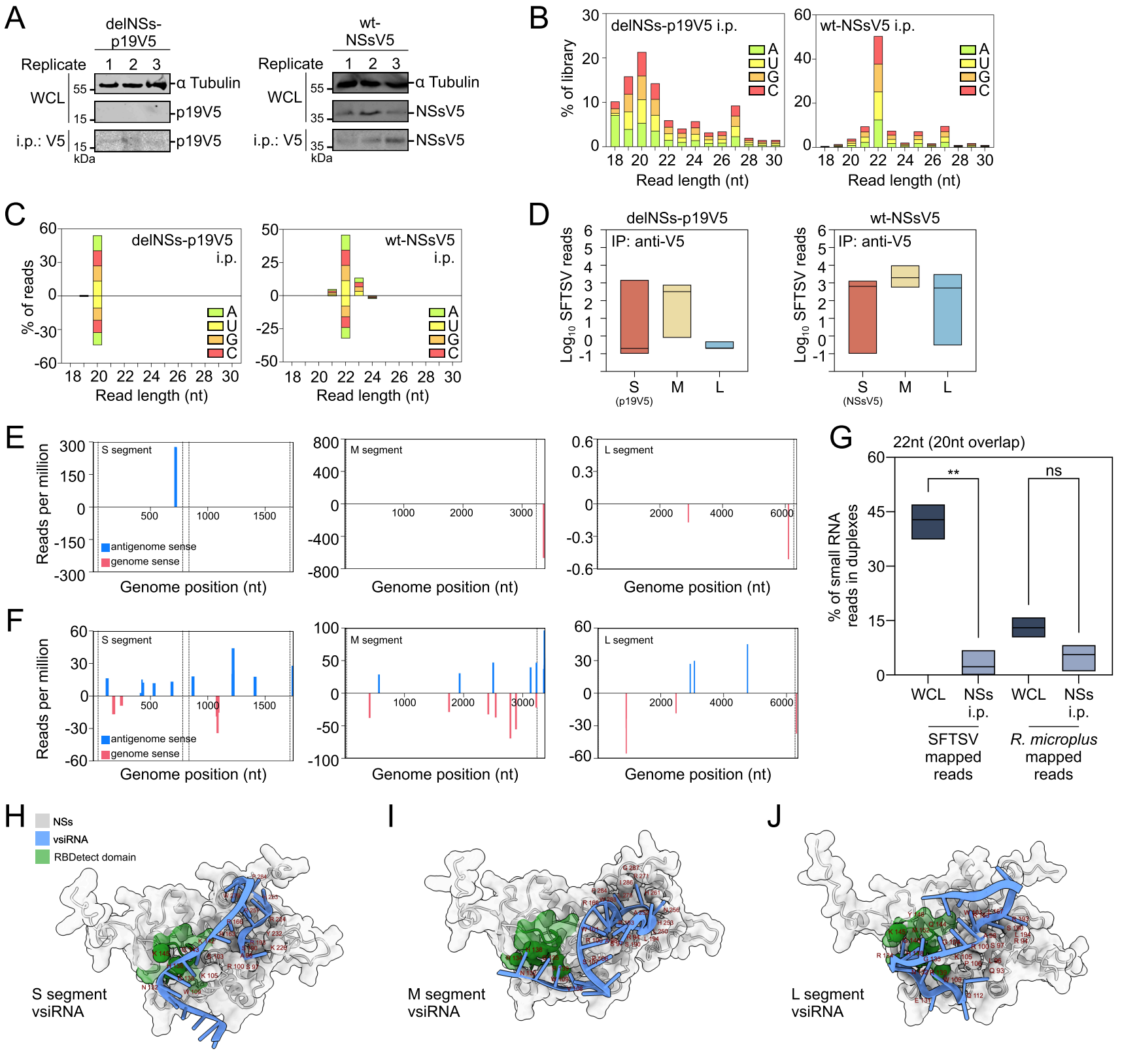
A
delNSs-p19V5
wt-NSsV5
Replicate 1 2 3
WCL
i.p.: V5
α Tubulin
p19V5
NSsV5
kDa
B
delNSs-p19V5 i.p.
wt-NSsV5 i.p.
% of library
Read length (nt)
A
U
G
C
C
delNSs-p19V5 i.p.
wt-NSsV5 i.p.
% of reads
D
delNSs-p19V5
wt-NSsV5
IP: anti-V5
Log10 SFTSV reads
S (p19V5)
M
L
S (NSsV5)
E
S segment
M segment
L segment
Reads per million
antigenome sense
genome sense
Genome position (nt)
F
G
22nt (20nt overlap)
% of small RNA reads in duplexes
**
ns
WCL
NSs i.p.
SFTSV mapped reads
R. microplus mapped reads
H
NSs
vsiRNA
RBDetect domain
S segment vsiRNA
I
M segment vsiRNA
J
L segment vsiRNA

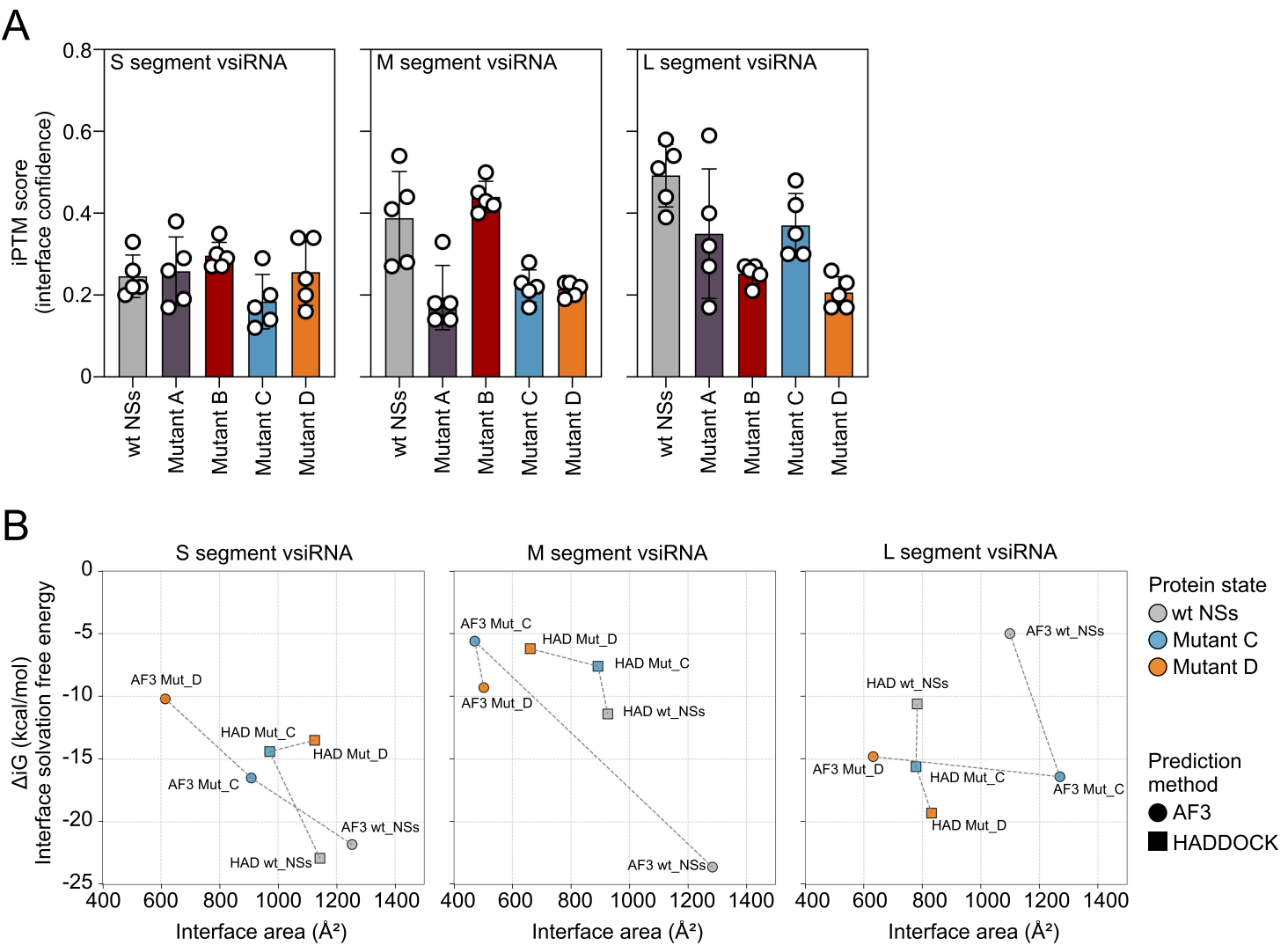
A
S segment vsiRNA
M segment vsiRNA
L segment vsiRNA
iPTM score
(interface confidence)
0.8
0.6
0.4
0.2
0
wt NSs
Mutant A
Mutant B
Mutant C
Mutant D
B
S segment vsiRNA
M segment vsiRNA
L segment vsiRNA
ΔiG (kcal/mol)
Interface solvation free energy
0
-5
-10
-15
-20
-25
400
600
800
1000
1200
1400
Interface area (Å²)
AF3 Mut_D
HAD Mut_C
HAD Mut_D
AF3 Mut_C
AF3 wt_NSs
HAD wt_NSs
Protein state
wt NSs
Mutant C
Mutant D
Prediction method
AF3
HADDOCK

Table 1. Design of SFTSV NSs RNA-binding interface mutants.

	Amino acid substitution			
	Arg100	Lys105	Arg139	Lys145
Mutant A	R > E		R > E	
Mutant B		K > E		K > E
Mutant C	R > E	K > E	R > E	K > E
Mutant D			R > E	K > E

Table summarising the panel of in silico–designed charge-reversal mutations introduced into SFTSV NSs to interrogate the predicted RNA-binding interface. Conserved basic residues (Arg100 [R], Lys105 [K], Arg139 [R], and Lys145 [K]) were individually or combinatorially substituted with glutamic acid [E] to disrupt electrostatic interactions with RNA. Mutants were designed to target residues within and adjacent to the predicted RNA-binding pocket, allowing assessment of the contribution of specific basic residues to RNA interaction without altering overall protein length or domain composition.